Prepared for submission to JCAP

Optimized dark matter searches in deep observations of Segue 1 with MAGIC

J. Aleksić[1,⋆] S. Ansoldi[2] L. A. Antonelli[3] P. Antoranz[4] A. Babic[5] P. Bangale[6] U. Barres de Almeida[6] J. A. Barrio[7] J. Becerra González[8,25] W. Bednarek[9] K. Berger[8] E. Bernardini[10] A. Biland[11] O. Blanch[1] R. K. Bock[6] S. Bonnefoy[7] G. Bonnoli[3] F. Borracci[6] T. Bretz[12,26] E. Carmona[13] A. Carosi[3] D. Carreto Fidalgo[12] P. Colin[6] E. Colombo[8] J. L. Contreras[7] J. Cortina[1] S. Covino[3] P. Da Vela[4] F. Dazzi[6] A. De Angelis[2] G. De Caneva[10] B. De Lotto[2] C. Delgado Mendez[13] M. Doert[14] A. Domínguez[15,27] D. Dominis Prester[5] D. Dorner[12] M. Doro[16] S. Einecke[14] D. Eisenacher[12] D. Elsaesser[12] E. Farina[17] D. Ferenc[5] M. V. Fonseca[7] L. Font[18] K. Frantzen[14] C. Fruck[6] R. J. García López[8] M. Garczarczyk[10] D. Garrido Terrats[18] M. Gaug[18] G. Giavitto[1] N. Godinović[5] A. González Muñoz[1] S. R. Gozzini[10] D. Hadasch[19] M. Hayashida[20] A. Herrero[8] D. Hildebrand[11] J. Hose[6] D. Hrupec[5] W. Idec[9] V. Kadenius[21] H. Kellermann[6] K. Kodani[20] Y. Konno[20] J. Krause[6] H. Kubo[20] J. Kushida[20] A. La Barbera[3] D. Lelas[5] N. Lewandowska[12] E. Lindfors[21,28] S. Lombardi[3,⋆] M. López[7] R. López-Coto[1] A. López-Oramas[1] E. Lorenz[6] I. Lozano[7] M. Makariev[22] K. Mallot[10] G. Maneva[22] N. Mankuzhiyil[2] K. Mannheim[12] L. Maraschi[3] B. Marcote[23] M. Mariotti[16] M. Martínez[1] D. Mazin[6] U. Menzel[6] M. Meucci[4] J. M. Miranda[4] R. Mirzoyan[6] A. Moralejo[1] P. Munar-Adrover[23] D. Nakajima[20] A. Niedzwiecki[9] K. Nilsson[21,28] K. Nishijima[20] N. Nowak[6] R. Orito[20] A. Overkemping[14] S. Paiano[16] M. Palatiello[2] D. Paneque[6] R. Paoletti[4] J. M. Paredes[23] X. Paredes-Fortuny[23] S. Partini[4] M. Persic[2,29] F. Prada[15,30] P. G. Prada Moroni[24] E. Prandini[16] S. Preziuso[4] I. Puljak[5] R. Reinthal[21] W. Rhode[14] M. Ribó[23] J. Rico[1,⋆] J. Rodriguez Garcia[6] S. Rügamer[12] A. Saggion[16] T. Saito[20] K. Saito[20] M. Salvati[3] K. Satalecka[7] V. Scalzotto[16] V. Scapin[7] C. Schultz[16] T. Schweizer[6]

A. Sillanpää[21] J. Sitarek[1] I. Snidaric[5] D. Sobczynska[9] F. Spanier[12] V. Stamatescu[1] A. Stamerra[3] T. Steinbring[12] J. Storz[12] S. Sun[6] T. Surić[5] L. Takalo[21] H. Takami[20] F. Tavecchio[3] P. Temnikov[22] T. Terzić[5] D. Tescaro[8] M. Teshima[6] J. Thaele[14] O. Tibolla[12] D. F. Torres[19] T. Toyama[6] A. Treves[17] M. Uellenbeck[14] P. Vogler[11] R. M. Wagner[6,31] F. Zandanel[15,32] R. Zanin[23] (the MAGIC Collaboration) and A. Ibarra[33]

[1]IFAE, Campus UAB, E-08193 Bellaterra, Spain

[2]Università di Udine, and INFN Trieste, I-33100 Udine, Italy

[3]INAF National Institute for Astrophysics, I-00136 Rome, Italy

[4]Università di Siena, and INFN Pisa, I-53100 Siena, Italy

[5]Croatian MAGIC Consortium, Rudjer Boskovic Institute, University of Rijeka and University of Split, HR-10000 Zagreb, Croatia

[6]Max-Planck-Institut für Physik, D-80805 München, Germany

[7]Universidad Complutense, E-28040 Madrid, Spain

[8]Inst. de Astrofísica de Canarias, E-38200 La Laguna, Tenerife, Spain

[9]University of Łódź, PL-90236 Lodz, Poland

[10]Deutsches Elektronen-Synchrotron (DESY), D-15738 Zeuthen, Germany

[11]ETH Zurich, CH-8093 Zurich, Switzerland

[12]Universität Würzburg, D-97074 Würzburg, Germany

[13]Centro de Investigaciones Energéticas, Medioambientales y Tecnológicas, E-28040 Madrid, Spain

[14]Technische Universität Dortmund, D-44221 Dortmund, Germany

[15]Inst. de Astrofísica de Andalucía (CSIC), E-18080 Granada, Spain

[16]Università di Padova and INFN, I-35131 Padova, Italy

[17]Università dell'Insubria, Como, I-22100 Como, Italy

[18]Unitat de Física de les Radiacions, Departament de Física, and CERES-IEEC, Universitat Autònoma de Barcelona, E-08193 Bellaterra, Spain

[19]Institut de Ciències de l'Espai (IEEC-CSIC), E-08193 Bellaterra, Spain

[20]Japanese MAGIC Consortium, Division of Physics and Astronomy, Kyoto University, Japan

[21]Finnish MAGIC Consortium, Tuorla Observatory, University of Turku and Department of Physics, University of Oulu, Finland

[22]Inst. for Nucl. Research and Nucl. Energy, BG-1784 Sofia, Bulgaria

[23]Universitat de Barcelona, ICC, IEEC-UB, E-08028 Barcelona, Spain

[24]Università di Pisa, and INFN Pisa, I-56126 Pisa, Italy

[25]now at: NASA Goddard Space Flight Center, Greenbelt, MD 20771, USA and Department of Physics and Department of Astronomy, University of Maryland, College Park, MD 20742, USA

[26]now at Ecole polytechnique fédérale de Lausanne (EPFL), Lausanne, Switzerland

[27]now at Department of Physics & Astronomy, UC Riverside, CA 92521, USA

[28]now at Finnish Centre for Astronomy with ESO (FINCA), Turku, Finland

[29]also at INAF-Trieste

[30]also at Instituto de Fisica Teorica, UAM/CSIC, E-28049 Madrid, Spain
[31]now at: Stockholm University, Oskar Klein Centre for Cosmoparticle Physics, SE-106 91 Stockholm, Sweden
[32]now at GRAPPA Institute, University of Amsterdam, 1098XH Amsterdam, Netherlands
[33]Physik-Department T30d, Technische Universität München, James-Franck-Straße, 85748 Garching, Germany
⋆corresponding author

E-mail: jelena@ifae.es, jrico@ifae, saverio.lombardi@pd.infn.it

Abstract. We present the results of stereoscopic observations of the satellite galaxy Segue 1 with the MAGIC Telescopes, carried out between 2011 and 2013. With almost 160 hours of good-quality data, this is the deepest observational campaign on any dwarf galaxy performed so far in the very high energy range of the electromagnetic spectrum. We search this large data sample for signals of dark matter particles in the mass range between 100 GeV and 20 TeV. For this we use the full likelihood analysis method, which provides optimal sensitivity to characteristic gamma-ray spectral features, like those expected from dark matter annihilation or decay. In particular, we focus our search on gamma-rays produced from different final state Standard Model particles, annihilation with internal bremsstrahlung, monochromatic lines and box-shaped signals. Our results represent the most stringent constraints to the annihilation cross-section or decay lifetime obtained from observations of satellite galaxies, for masses above few hundred GeV. In particular, our strongest limit (95% confidence level) corresponds to a ∼500 GeV dark matter particle annihilating into $\tau^+\tau^-$, and is of order $\langle\sigma_{\rm ann}v\rangle \simeq 1.2\times10^{-24}$ cm^3 s^{-1} – a factor ∼40 above the $\langle\sigma_{\rm ann}v\rangle$ thermal value.

Keywords: dark matter, indirect searches, gamma-ray experiments, Imaging Air Cherenkov Telescopes, dwarf spheroidal galaxies, Segue 1

Contents

1 Introduction

Dark matter (DM) is an, as yet, unidentified type of matter, which accounts for about 85% of the total mass content and 26% of the total energy density of the Universe [1]. Despite the abundant evidence on all astrophysical length scales implying its existence, the nature of DM is still to be determined. Observations require the DM particles to be electrically neutral, non-baryonic and stable on cosmological time scales. Furthermore, in order to allow the small-scale structures to form, these particles must be "cold" (i.e. non-relativistic) at the onset of structure formation. However, a particle fulfilling all those requirements does not exist within the Standard Model (SM); thus, the existence of DM inequivocally points to new physics. A particularly well motivated class of cold DM candidates are the weakly interacting massive particles (WIMPs, [2]). WIMPs are expected to have a mass in the range between $\sim$10 GeV and a few TeV, interaction cross-sections typical of the weak scale and they naturally provide the required relic density ("WIMP miracle", see, e.g., [3]). Several extensions of the SM include WIMP candidates, most notably Supersymmetry (see, e.g., [4]), as well as theories with extra dimensions [5], minimal SM extensions [6], and others (for a review see, e.g., [3]).

The search for WIMPs is conducted on three complementing fronts, namely: production in particle accelerators, direct detection in underground experiments and indirect detection. The latter implies the searches, by ground- and space-based observatories, of the SM particles presumably produced in WIMP annihilations or decays. Accelerator and direct detection experiments are most sensitive to DM particles with mass below a few hundred GeV. Positive results for signals of ∼10 GeV DM reported by some direct-searches experiments [7–10] could not be confirmed by other detectors, and are in tension with results obtained by XENON100 [11, 12] and LUX [13]. On the other hand, the rather heavy Higgs boson [14] and the lack of indications of new physics at the Large Hadron Collider, strongly constrain the existence of a WIMP at the electroweak scale. Therefore, the current status of these experimental searches strengthens the motivation for DM particles with masses at the TeV scale or above – the mass range best (and sometimes exclusively) covered by the Imaging Air Cherenkov Telescopes (IACTs). For this reason, IACT observations in the very high energy domain (E $\gtrsim$ 100 GeV) provide extremely valuable clues to unravel the nature of the DM. Such searches are the primary scope of this work.

Among the best-favored targets for indirect DM detection with gamma-ray observatories are dwarf spheroidal galaxies (dSphs). The dSph satellites of the Milky Way are relatively close-by (less than a few hundred kpc away), and in general less affected by contamination from gamma rays of astrophysical origin than some other DM targets, like the Galactic Center (GC) and galaxy clusters (see, e.g, [15, 16]). Furthermore, given the low baryonic content and large amounts of DM expected in these kind of galaxies, dSphs are considered highly promising targets for indirect DM searches. Over the last decade, a number of dSphs have been observed by the present generation of IACTs: MAGIC [17–19], H.E.S.S. [20–22] and VERITAS [23, 24], as well as by the Large Area Telescope (LAT) on board the *Fermi* satellite [25].

In this work we present the results of deep observations of the dSph galaxy Segue 1 with MAGIC. Discovered in 2006 in the imaging data from the Sloan Digital Sky Survey [26], Segue 1 is classified as an ultra-faint dSph, of absolute magnitude $M_V = -1.5^{+0.6}_{-0.8}$. With a mass-to-light ratio estimated to be ∼3400 $M_\odot/L_\odot$ [27], this is the most DM-dominated object known so far. Furthermore, given its relative closeness (23±2 kpc), lack of backgrounds of conventional origin, high expected DM flux and its favorable position in the Northern hemisphere and outside of the Galactic plane (RA, DEC = 10.12^h, 16.08°), Segue 1 has been selected as an excellent target for DM searches with MAGIC.

We present the results of a three-year long (2011–2013) observational campaign on Segue 1 carried out with MAGIC in stereoscopic mode. With almost 160 hours of good-quality data, this is the deepest exposure of any dSph by any IACT so far. No significant gamma-ray signal is found. The gathered data are used to set constraints on various models of DM annihilation and decay, providing the most sensitive indirect DM search on dSphs for the WIMP mass range between few hundred GeV and 10 TeV. In particular, we improve our previous limits, obtained from ∼30 hours of Segue 1 observations in the single telescope mode [19], by one order of magnitude. This improvement is achieved through the increased sensitivity of the MAGIC stereo system, the deep exposure, and the use of the *full likelihood analysis* [28] – a method optimized for searches of characteristic, DM-induced gamma-ray spectral features.

This paper is structured as follows: first, we describe the observations of Segue 1 with MAGIC, data reduction and standard analysis procedures (section 2). Then, in section 3, we describe the basics of the full likelihood method, used for the analysis of our data, and

	Sample A	**Sample B1**	**Sample B2**	**Sample C**
Readout	DRS2	DRS4	DRS4	DRS4
MAGIC-I camera	old	old	old	new
Obs. period	Jan–May 2011	Jan–Feb 2012	Mar–May 2012	Nov 2012–Feb 2013
Obs. time [h]	64	24.28	59.77	55.05
Zd range [deg]	13–33.7	13–32.5	13–35.7	13–37
Az range [deg]	104.8–250.2	120.2–252.0	115.4–257.2	103.8–259.4
Wobble around	dummy	dummy	dummy	Segue 1
Wobble offset [deg]	0.29	0.29	0.29	0.40
W1 $t_{\rm eff}$ [h]	22.66	6.07	25.02	23.71
W2 $t_{\rm eff}$ [h]	24.35	6.20	26.11	23.80
$t_{\rm eff}$ [h]	47.00	12.26	51.13	47.51
Total $t_{\rm eff}$ [h]				**157.9**

Table 1: Basic details of the Segue 1 observational campaign with MAGIC. Refer to the main text for additional explanations.

the particular choices we have made regarding the likelihood construction. In section 4 we give details on the expected photon flux from DM annihilation and decay, with accent on the spectral shapes of the considered models and the calculations of the astrophysical term of the flux. Section 5 presents our results – the upper limits on annihilation cross section and lower limits on the DM particle lifetime for the studied channels, and in section 6 those are put into context and compared with constraints from other gamma-ray experiments. Lastly, section 7 summarizes this paper and our conclusions.

2 Observations and conventional data analysis

The *Florian Goebel* Major Atmospheric Gamma-ray Imaging Cherenkov (MAGIC) Telescopes are located at the Roque de los Muchachos Observatory (28.8° N, 17.9° W; 2200 m a.s.l.) on the Canary Island of La Palma, Spain. The system consists of two, 17 m diameter telescopes with fast imaging cameras of 3.5° field of view. The first telescope, MAGIC-I, has been operational since 2004, and in 2009 it was joined by MAGIC-II. The trigger threshold of the system is ∼50 GeV for the standard observations; the integral sensitivity above 250 GeV, for 5σ detection in 50 hours, is ∼0.7% of the Crab Nebula flux, with an angular resolution better than 0.07° (39% containment radius, [29]).

Observations of Segue 1 were performed between January 2011 and February 2013. During this period, the MAGIC Telescopes underwent a series of important hardware changes, aimed at the homogenization and improvement of the performance of both instruments [29]. First, at the end of 2011, the readout electronics of the telescopes were upgraded to the Domino Ring Sampler version 4 (DRS4)-based readouts, thus reducing the dead time of 0.5 ms (introduced by the previously used DRS2-based readout electronics in MAGIC-II) to 26 μs [30]. Second, by the end of 2012, the camera of MAGIC-I was exchanged with a replica of that of MAGIC-II, with uniform pixel size and extended trigger area with respect to the old camera [31].

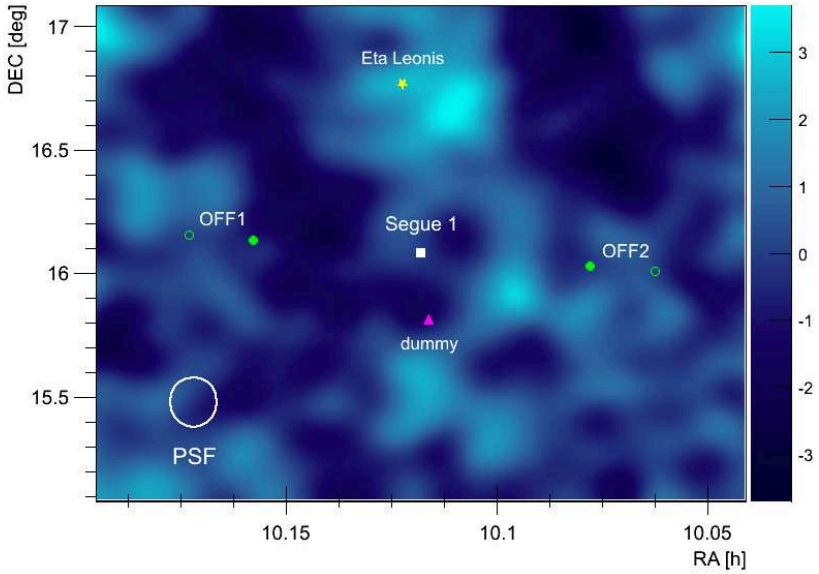

Figure 1: Segue 1 significance skymap above 150 GeV, from 157.9 hours of observations. Nominal positions of Segue 1 and η Leo are marked with the square and the star, respectively. Also shown is the wobbling scheme used in different samples: for periods A, B1 and B2 the wobbling was performed with respect to the 'dummy' position (triangle), and around Segue 1 for period C, while the centers of the *OFF* regions were used for background estimation at the position of the source (full circles for periods A, B1 and B2, and empty circles for period C). Positions of the camera center are found at an equal distance from Segue 1 and the respective *OFF* positions, and are not shown here. See the main text for more details.

Due to the upgrade, the response of the telescopes varied throughout the Segue 1 campaign. Consequently, we have defined four different observational samples, such that for each of them the performance and response of the instruments are considered stable. Sample A corresponds to the beginning of the campaign in 2011, before the upgrade started. Samples B1 and B2 refer to the first half of 2012, when both telescopes were operating with new, DRS4-based readouts. B1 corresponds to the commissioning phase after the first upgrade, and is affected by several faulty readout channels, which were fixed for period B2. Finally, sample C was obtained at the end of 2012 and beginning of 2013, with the final configuration of the system including the new camera of MAGIC-I. Table 1 summarizes the relevant observational parameters of each of the four periods. Each sample has been processed separately, with the use of contemporaneous Crab Nebula observations (for optimization of the analysis cuts and validation of the analysis procedures) and dedicated Monte Carlo productions (for evaluation of the response of the instruments).

The data taking itself was performed in the so-called wobble mode [32], using two pointing (wobble) positions. The residual background from Segue 1 (*ON* region) was estimated for each of the two pointings (W1 and W2) separately, using an *OFF* region placed at the same relative location with respect to the center of the camera as the *ON* region, but from the complementary wobble observation. To ensure a homogeneous ON/OFF acceptance, special care was taken during the data taking to observe both wobble positions for similar amounts of time within similar azimuthal (Az) ranges. For periods A, B1 and B2, in order to exclude the nearby, 3.5-apparent magnitude star η Leo from the trigger area of MAGIC-I old camera, the wobbling was done with respect to a 'dummy' position located 0.27° away from Segue 1 and on the opposite side with respect to η Leo (figure 1). With wobbling done

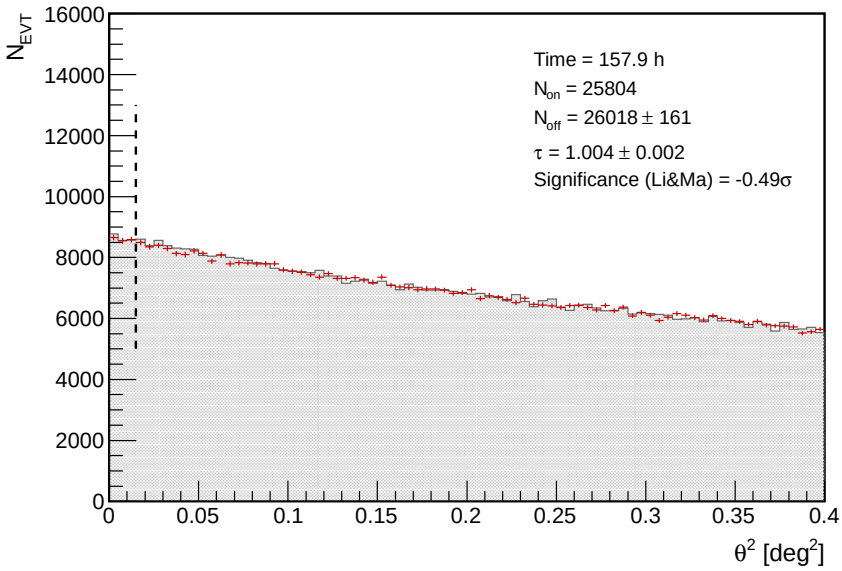

Figure 2: Segue 1 θ^2 distribution above 60 GeV, from 157.9 hours of observations. The signal (*ON* region) is presented by red points, while the background (*OFF* region) is the shaded gray area. The *OFF* sample is normalized to the *ON* sample in the region where no signal is expected, for θ^2 between 0.15 and 0.4 deg^2. The vertical dashed line shows the $\theta^2_{\rm cut}$ value.

at an offset of 0.29°, in a direction approximately perpendicular to the one joining η Leo and Segue 1, the pointing positions were ∼0.4° and ∼1° away from the potential source and the star, respectively. For period C, with the new MAGIC-I camera, the star could no longer be excluded from its extended trigger area, so the standard observational scheme was used instead: the wobble positions were chosen at the opposite sides of Segue 1, at an 0.4° offset and in a direction parallel to the one used for the A, B1 and B2 samples.

Data reduction was performed using the standard MAGIC analysis software MARS [33]. Data quality selection was based mainly on stable trigger rates, reducing the total sample of 203.1 hours of observations to 157.9 hours of good quality data (see table 1 for total and effective observation times ($t_{\rm eff}$) of each of the four samples). For the data analysis, after the image cleaning, we retain only events with a *size* (total signal inside the shower) larger than 50 photo-electrons in each telescope and reconstructed energy greater than 60 GeV. Furthermore, for every event, we calculate the angular distance θ between the reconstructed arrival direction and the *ON* (or *OFF*) center position, as well as the signal-to-noise maximization variable *hadronness* (h) by means of the Random Forest method [34], and select events with $\theta^2 < \theta^2_{\rm cut}$ and $h < h_{\rm cut}$. The values of $\theta^2_{\rm cut}$ and $h_{\rm cut}$ are optimized on the contemporaneous Crab Nebula data samples, by maximizing the expected integral flux sensitivity (according to Li & Ma [35]) in the whole energy range. For all four of the considered data samples, we obtain $\theta^2_{\rm cut} = 0.015$ deg^2 [1], whereas for $h_{\rm cut}$ we get 0.30 for samples A and B1, and 0.25 for samples B2 and C.

Additionally, the effect that η Leo has on the data was also taken into account. Namely,

[1] We note that the $\theta^2_{\rm cut}$ is optimized for a point-like source, whereas Segue 1 is slightly extended for MAGIC (see section 4.2). We have confirmed that the sensitivity could be improved by up to 10% for $\theta^2_{\rm cut}$ values slightly larger than the selected ones. This, however, would have been at the expense of background modeling (the number of available modeling zones would be reduced, see section 3), thus this option was disregarded.

pixels illuminated by the star produce background triggers with a rate larger than those due to atmospheric showers. To avoid the saturation of the data acquisition with such events, the thresholds of the affected pixels are automatically increased/decreased with the rotation of the star in the camera. As a consequence, a region is created around the η Leo position where the efficiency for shower detection is reduced with respect to the nominal one. This causes differences between the spatial distributions of events with respect to the *ON* and *OFF* positions, which could introduce inhomogeneities in the instrument response function across the field of view. In our Segue 1 observations, this effect is only significant for sample C (because the star is closer to the camera center). We restore the *ON*-*OFF* symmetry by removing those events of reconstructed energy lower than 150 GeV and for which the center of gravity of the shower image, in either one of the cameras, lies less than 0.2° away from the position of η Leo (or from a position at the same relative location with respect to the *OFF* region as the star is from the *ON* region). The optimization of these energy and angular distance cuts was done by imposing agreement between *ON* and *OFF* θ^2-distributions for events with $0.35 < h < 0.60$ (i.e. excluding those selected as the signal candidates). The corresponding Monte Carlo production was treated with the same star-related cuts.

Figure 1 represents the skymap centered at Segue 1: no significant gamma-ray excess can be seen at its nominal position. The same conclusion is made from the overall θ^2-distribution (figure 2). Consequently, we proceed to calculate the differential and integral flux upper limits for the gamma-ray emission from the potential source, by means of the *conventional* analysis approach (for details and formalism, see [28]), currently standard for IACTs. However, as it has been shown that the conventional method is suboptimal to the full likelihood analysis for spectral emissions with known characteristic features (as expected from gamma-rays of DM origin, [28]), those upper limits are quoted for completeness and cross-checking purposes only and can be found in Appendix A. The actual analysis of the Segue 1 data proceeds with the full likelihood method, and more details on it are provided in the following section.

3 Full likelihood analysis

As shown by Aleksić, Rico and Martinez in [28], the full likelihood approach maximizes the sensitivity to gamma-ray signals of DM origin by including the information about the expected spectral shape (which is fixed for a given DM model) into the calculations. The sensitivity improvement obtained by the use of this method is predicted to be a factor ∼(1.5–2.5) with respect to the conventional analysis (depending on the spectral form of the searched signal).

In this work, we present the results of the full likelihood analysis applied to our Segue 1 observations with MAGIC. We follow the formalism and nomenclature defined in [28] (for the Reader's convenience, also included below), and address our specific choices for the different terms entering the likelihood in more detail.

The basic concept behind the method is the comparison of the *measured* and *expected* spectral distributions; that is, we have to model the emission expected from the *ON* region. For a given DM model, M, the spectral shape is known (see section 4), thus the only free parameter is the intensity of the gamma-ray signal (θ). The corresponding likelihood function has the following form:

$$\mathcal{L}(N_{\rm EST}, M(\theta)|N_{\rm OBS}, E_1, ..., E_{N_{\rm OBS}}) = \frac{{N_{\rm EST}}^{N_{\rm OBS}}}{N_{\rm OBS}!} e^{-N_{\rm EST}} \times \prod_{i=1}^{N_{\rm OBS}} \mathcal{P}(E_i; M(\theta)), \qquad (3.1)$$

with $N_{\rm OBS}(= N_{\rm ON} + N_{\rm OFF})$ and $N_{\rm EST}$ denoting the total number of observed and estimated events, respectively, in *ON* and *OFF* regions. $\mathcal{P}(E_i; M(\theta))$ is the value of the probability density function of the event i with *measured* energy E_i:

$$\mathcal{P}(E; M(\theta)) = \frac{P(E; M(\theta))}{\int_{E_{\rm min}}^{E_{\rm max}} P(E; M(\theta)) dE}, \tag{3.2}$$

where $E_{\rm min}$ and $E_{\rm max}$ are the lower and upper limits of the considered energy range. $P(E; M(\theta))$ represents the differential rate of the events, such that:

$$P(E; M(\theta)) = \begin{cases} P_{\rm OFF}(E_i), & i \in OFF \\ P_{\rm ON}(E_i; M(\theta)), & i \in ON \end{cases}, \tag{3.3}$$

where $P_{\rm OFF}(E)$ and $P_{\rm ON}(E; M(\theta))$ are the expected differential rates from the *ON* and *OFF* regions. In this work, $P_{\rm OFF}(E)$ is determined from the data (see bellow), whereas $P_{\rm ON}(M(\theta); E)$ is calculated as:

$$P_{\rm ON}(E; M(\theta)) = \frac{1}{\tau} P_{\rm OFF}(E) + \int_0^\infty \frac{d\Phi(M(\theta))}{dE'} R(E; E') dE'. \tag{3.4}$$

True energy is denoted with E'; $d\Phi(M(\theta))/dE'$ is the predicted differential gamma-ray flux, and $R(E; E')$ is the response function of the telescope. Lastly, τ refers to the normalization between *OFF* and *ON* regions.

Thus, in practice, for the construction of the full likelihood function, we need the instrument response to gamma-ray events, a model of the background differential rate, and an assumed signal spectrum:

- the instrumental response function ($R(E; E')$) can be described by the effective collection area ($A_{\rm eff}$) and by the energy dispersion function. The latter is well approximated, for a given E', with a Gaussian, whose mean and width will be referred to as the energy bias and resolution, respectively. For each of the four observational periods, the response functions are independently determined from the corresponding Monte Carlo simulations;

- the model of the background differential rate ($P_{\rm OFF}(E)$) is obtained, for each period and each wobble pointing, directly from the Segue 1 observations at the complementary wobble position. For each pointing we select four model regions that have similar exposure as the *OFF* region, and we define them to be of the same angular size and at the same angular distance from the camera center as the corresponding *OFF* region, and adjacent to it. Then, by the means of the Kolmogorov-Smirnov statistics (K-S), we compare the energy distribution of events from each of the modeling zones (individually and combined) to that from the *OFF* region. The modeling region(s) providing the highest K-S probability is (are) selected, and its (smoothed) measured differential energy distribution is used as the background model in the full likelihood (for more details, refer to [37]). The statistical and systematic uncertainties introduced by this procedure in our final results are estimated by comparing the limits obtained using the selected modeling region(s) with those that we would obtain if the average of all four zones was used instead. Our constraints on DM properties are found to vary by up to 10% for the considered range of DM particle masses.

- the signal spectral function ($d\Phi(M(\theta))/dE'$) is known and fixed for a given DM model. In this work, we consider several channels of photon production from DM annihilation or decay: secondary photons from SM final states, gamma-ray lines, virtual internal bremsstrahlung (VIB) photons and gamma-ray boxes. More details on these final states are provided in section 4.1.

For each of the two pointing positions of each of the four defined observational periods, an individual likelihood function is constructed using the corresponding background model, plus the signal spectral function convoluted with the appropriate response of the telescopes. The global likelihood, encompassing the entire Segue 1 data sample, is obtained as a product of those individual ones (eq. (5.1) in [28]). It is maximized with the gamma-ray signal intensity as a free parameter, while $N_{\rm EST}$ and τ of each individual sample are treated as nuisance parameters with Poisson and Gaussian distributions, respectively. The free parameter is bounded to the physical region during the likelihood maximization: that is, the signal intensity is not allowed to take negative values. We note that the results obtained this way are conservative (i.e. they may have a slight over-coverage, see [36]), since negative fluctuations cannot produce artificially constraining limits.

The full likelihood calculations are performed for the 95% confidence level (CL) and one-sided confidence intervals ($\Delta \log \mathcal{L} = 1.35$) using the `TMinuit` class of ROOT [38].

4 Expected dark matter flux

Before proceeding to the results of the full likelihood analysis of our Segue 1 sample, let us first comment on how the limits on the DM-induced gamma-ray signal are translated to limits on DM properties.

The prompt gamma-ray flux produced in annihilation or decay of DM particles is given as a product of two terms:

$$\frac{d\Phi(\Delta\Omega)}{dE'} = \frac{d\Phi^{\rm PP}}{dE'} \times J(\Delta\Omega). \tag{4.1}$$

The particle physics term, $d\Phi^{\rm PP}/dE'$, solely depends on the chosen DM model – it is completely determined for the given theoretical framework and its value is the same for all sources. The astrophysical term, $J(\Delta\Omega)$, on the other hand, depends on the observed source (its distance and geometry), the DM distribution at the source region and the properties of the instrument and the analysis.

In the case of *annihilating* DM, the particle physics term takes the form:

$$\frac{d\Phi^{\rm PP}}{dE'} = \frac{1}{4\pi}\frac{\langle\sigma_{\rm ann}v\rangle}{2m_\chi^2}\frac{dN}{dE'}, \tag{4.2}$$

where m_χ is the DM particle mass, $\langle\sigma_{\rm ann}v\rangle$ is the thermally averaged product of the total annihilation cross-section and the velocity of the DM particles, and $dN/dE' = \sum_{i=1}^{n} {\rm Br}_i dN_i/dE'$ is the differential gamma-ray yield per annihilation, summed over all the n possible channels that produce photons, weighted by the corresponding branching ratio Br. All the information regarding the spectral shape is contained in the dN/dE' term.

On the other hand, the astrophysical factor ($J_{\rm ann}$) is the integral of the square of the DM density (ρ) over the line of sight (los) and the solid angle covered by the observations ($\Delta\Omega$), i.e.:

$$J_{\rm ann}(\Delta\Omega) = \int_{\Delta\Omega}\int_{los} \rho^2(l,\Omega) dl d\Omega. \tag{4.3}$$

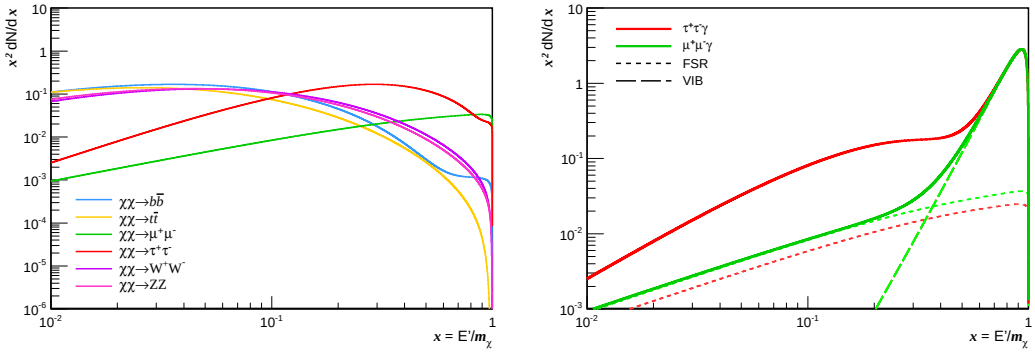

Figure 3: Gamma-ray spectrum for DM annihilation into different final states. (**Left**) Secondary photons (when applicable, the FSR is included in the spectrum). Modeling is done according to the fits provided in [39]. (**Right**) Spectral distribution from annihilation into leptonic three-body final states (solid lines), with the contributions from FSR and VIB photons (dashed and long-dashed lines, respectively). The assumed mass-splitting parameter value is $\mu = 1.1$.

For the case of *decaying* DM, the particle physics term depends on the lifetime of the particle τ_χ, and its form is obtained by replacing the $\langle\sigma_{\rm ann}v\rangle/2m_\chi$ contribution with $1/\tau_\chi$ in eq. (4.2). As for the astrophysical term ($J_{\rm dec}$), it scales linearly with the DM density ($\rho^2 \to \rho$ in eq. (4.3)).

We express the results of our DM searches as upper limits to $\langle\sigma_{\rm ann}v\rangle$ (for the annihilation scenarios) or as lower limits to τ_χ (for the decaying DM). In the full likelihood analysis, $\langle\sigma_{\rm ann}v\rangle$ or τ_χ play the role of the free parameter.

4.1 Considered spectral shapes

As already mentioned in section 3, in this work we search for DM annihilating or decaying into different final states. In particular, we consider the following channels: $b\bar{b}$, $t\bar{t}$, $\mu^+\mu^-$, $\tau^+\tau^-$, W^+W^- and ZZ. The resulting spectra from secondary photons are continuous and rather featureless, with a cutoff at the kinematical limit $E' = m_\chi$ (figure 3-left). In our analysis, we use the parametrization presented in [39]. When applicable, the final state radiation (FSR) contribution is included in those fits.

We also analyze final states leading to sharp spectral features. First, we consider the direct annihilation into two photons ($\chi\chi \to \gamma\gamma$), or a photon and a boson ($\chi\chi \to \gamma Z/h$). Although loop-suppressed ($\sim \mathcal{O}(1/\alpha^2)$), such processes are of great interest, as they would result in a sharp, monochromatic line-like feature in the photon spectrum – a feature whose detection would represent the smoking gun for DM searches. Such a line is described as:

$$\frac{dN}{dE'} = N_\gamma \delta(E' - E_0), \tag{4.4}$$

where $E_0 = m_\chi$ and $N_\gamma = 2$ for annihilation into $\gamma\gamma$, while $E_0 = m_\chi(1 - M^2_{Z/h}/4m^2_\chi)$ and $N_\gamma = 1$ for annihilation into $\gamma Z/h$. In the latter case, there is also a contribution to the gamma-ray spectrum originated in the fragmentation and decay of the Z and Higgs bosons. As for the case of the decaying DM, line production is also a possibility. In this work, we consider the case of two-body decay into one monoenergetic photon ($\chi \to \gamma\nu$) for fermionic DM particles. The spectral function of the resulting line is obtained by simply making the substitution $m_\chi \to m_\chi/2$ in eq. (4.4).

Another scenario resulting in sharp spectral features involves emission of VIB photons: if the DM particle is a Majorana fermion, which couples via a Yukawa coupling to a charged fermion (f) and a scalar (η), the photon produced in the internal bremsstrahlung process ($\chi\chi \to f\bar{f}\gamma$) will have a very characteristic spectrum, displaying a salient feature close to the kinematic endpoint and resembling a distorted gamma-ray line. The exact expression of the differential gamma-ray spectrum of the 2→3 process is given by eq. (2.8) in [43]. The total spectral distribution also receives a contribution from FSR of the nearly on-shell fermions produced in the 2→2 annihilation ($\chi\chi \to f\bar{f}$), as well as from the fragmentation or decay of the fermions produced both in the 2→2 and in the 2→3 processes (figure 3-right). The contribution from FSR becomes more and more important as the mass splitting μ ($\equiv m_\eta^2/m_\chi^2$) between η and the DM particle increases, eventually erasing the strong gamma-ray feature from internal bremsstrahlung. It can be verified that the gamma-ray feature stands out in the total spectrum when $\mu \lesssim 2$, which is the case we assume in our analysis.

Lastly, a sharp feature might arise in scenarios where a DM particle annihilates into an on-shell intermediate scalar ϕ, which subsequently decays in flight into two photons: $\chi\chi \to \phi\phi \to \gamma\gamma\gamma\gamma$. In the rest frame of ϕ, photons are emitted isotropically and monoenergetically; therefore, in the galactic frame, the resulting spectrum will be box-shaped (for the exact expression for dN/dE', see eq. (2) in [44]). The center and width of such a feature are completely determined by the masses of the scalar (m_ϕ) and DM particle: the box is centered at $E' = m_\chi/2$ and its width is $\Delta E' = \sqrt{m_\chi^2 - m_\phi^2}$. For $m_\phi \approx m_\chi$, almost all of the DM particle energy is transferred to the photons, and the resulting spectral shape is intense and similar to the monochromatic line. On the other hand, for $m_\phi \ll m_\chi$ the box becomes wide and dim in amplitude; still, it extends to higher energies and thus is not negligible as a contribution to the signal spectrum.

4.2 The astrophysical factor J for Segue 1

The choice of density profile plays a crucial role in the calculation of the astrophysical factor J, as it has direct implications on the expected photon flux. This is particularly true for DM annihilation (eq. (4.3)): as $J_{\rm ann}$ is proportional to ρ^2, cored central distributions (described by a constant density value close to the center) will yield lower fluxes than the cusped ones (described by a steep power law in the central region), for the same total DM content. This dependence is less pronounced for the decaying DM, since $J_{\rm dec} \propto \int \rho$. Motivated by the numerical simulations, we model the DM density distribution assuming the Einasto profile [45], with scale radius $r_s = 0.15$ kpc, scale density $\rho_s = 1.1{\times}10^8\ M_\odot\ {\rm kpc}^{-3}$ and slope $\alpha = 0.30$ [19, 40].

The value of J is determined by the DM distribution within the integrated solid angle $\Delta\Omega$ (eq. (4.3)), and hence by the analysis angular cut $\theta^2_{\rm cut}$ (figure 4-left). In addition, in order to compute the residual background in the *ON* region, we measure the number of events acquired in the *OFF* regions, defined by the same $\theta^2_{\rm cut}$ and at an angular distance from the position of Segue 1 of $\Phi = 0.58^\circ$ (for samples A, B1 and B2) and $\Phi = 0.80^\circ$ (for sample C). The *OFF* regions may contain non-negligible amounts of DM-induced events (figure 4-right), which are accounted in the analysis as background, hence reducing the sensitivity for detection of signal events in the *ON* region. We take this into account by using the difference in J between *ON* and *OFF* regions as astrophysical factor, that is: $J(\Delta\Omega) = J^{\rm ON}(\Delta\Omega) - J^{\rm OFF}(\Delta\Omega)$. This correction is negligible (less than 1%) for annihilation, but has an effect of ∼10% for decay, since in this case the abundant, although less concentrated quantities of DM at large Φ contribute relatively more to the total expected flux than in the case of

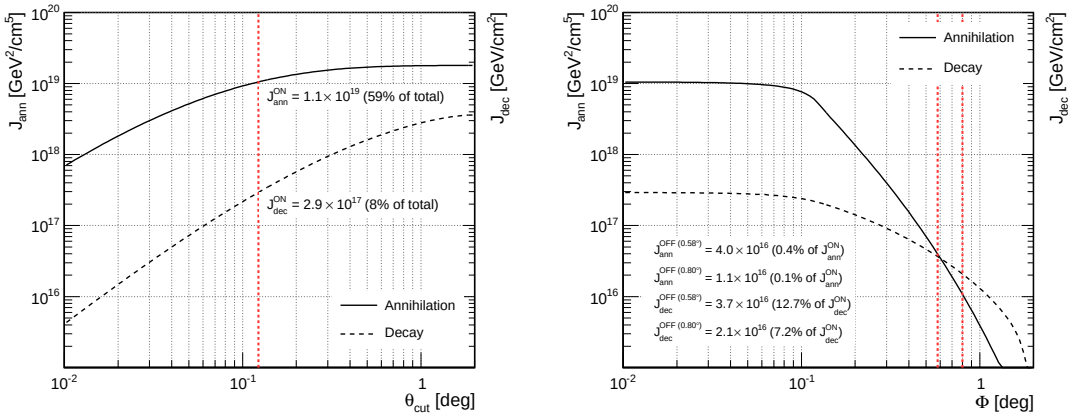

Figure 4: Astrophysical factor for Segue 1 for annihilating ($J_{\rm ann}$, solid line, left axis) and decaying ($J_{\rm dec}$, dashed line, right axis) DM, assuming the Einasto density profile. (**Left**): as a function of the angular cut ($\theta^2_{\rm cut}$, see section 2), for observations centered at the nominal position of Segue 1. The vertical dotted red line corresponds to the value used in this analysis, $\theta^2_{\rm cut} = 0.015^\circ$. (**Right**) as a function of the angular distance from Segue 1 (Φ), for a fixed anglar cut $\theta^2_{\rm cut} = 0.015^\circ$. The vertical dotted red lines correspond to the values of distance between the *ON* and *OFF* regions relevant in this analysis.

annihilation. For the angular cut $\theta^2_{\rm cut} = 0.015^\circ$ and the used *OFF* positions, the astrophysical factor for annihilating DM is $J_{\rm ann} = 1.1{\times}10^{19}$ GeV^2 cm^{-5}, and the corresponding values for decay are $J_{\rm dec} = 2.5{\times}10^{17}$ GeV cm^{-2} for periods A, B1 and B2, and $J_{\rm dec} = 2.7{\times}10^{17}$ GeV cm^{-2} for period C.

The dominating systematic uncertainty on J, resulting from the fit of the Segue 1 DM distribution to the Einasto profile, is about a factor of 4 at 1σ level for $J_{\rm ann}$, and about a factor of 2 for $J_{\rm dec}$ [40]. These uncertainties affect our $\langle\sigma_{\rm ann}v\rangle$ and τ_χ limits linearly. A discussion about comparisons of J uncertainties for different classes of objects is included in section 6.2.

5 Limits for dark matter annihilation and decay models

Here we present the results, in the context of indirect DM searches, of 157.9 hours of selected data from the Segue 1 observations with MAGIC, analyzed with the full likelihood approach. The results are introduced in the following way: for each of the considered DM models, a limit is set (95% CL upper limit on $\langle\sigma_{\rm ann}v\rangle$ or lower limit on τ_χ) by using the combined likelihood for the whole data sample. This constraint is then compared to the expectations for the null hypothesis (no signal), as well as for signals of 1σ and 2σ significances, estimated from the fast simulations (comparison with negative signals is meaningless in this work, as the free parameter is constrained to only have positive values, see section 3). In order to make the results as model-independent as possible, in all the cases, the branching ratio is set to Br = 100%. Considering the energy range for which the MAGIC telescopes are sensitive to gamma rays, we search for DM particles of mass m_χ between 100 GeV and 10 TeV for annihilation scenarios and between 200 GeV and 20 TeV for the decaying DM. Furthermore, all of the results are produced without the assumptions of some additional boosts, either from the presence of substructures [41] or from quantum effects [42].

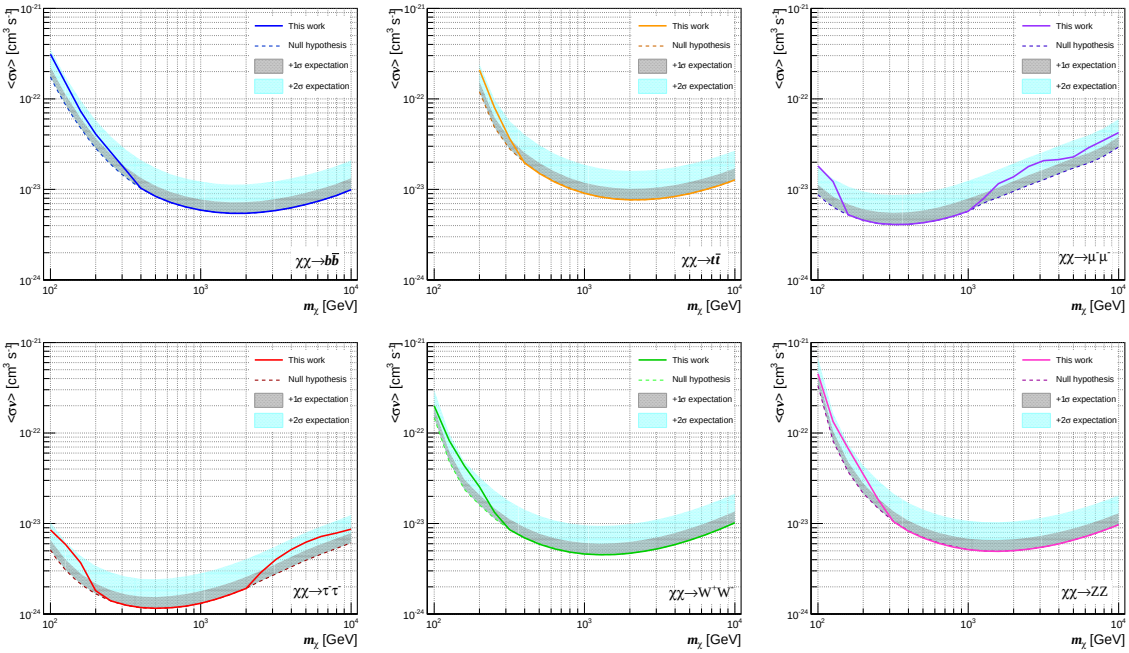

Figure 5: Upper limits on $\langle\sigma_{\rm ann}v\rangle$ for different final state channels (from top to bottom and left to right): $b\bar{b}$, $t\bar{t}$, $\mu^+\mu^-$, $\tau^+\tau^-$, W^+W^- and ZZ, from the Segue 1 observations with MAGIC. The calculated upper limit is shown as a solid line, together with the null-hypothesis expectations (dashed line), and expectations for 1σ (shaded gray area) and 2σ (shaded light blue area) significant signal.

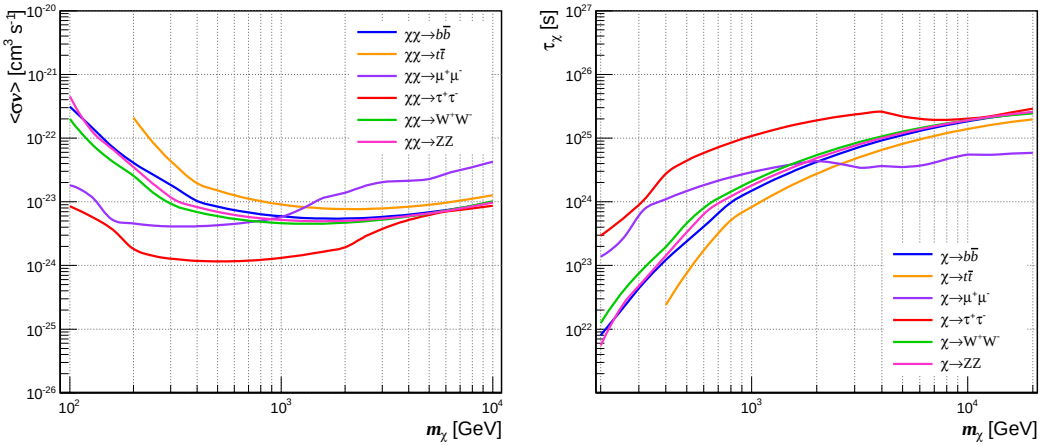

Figure 6: Upper limits on $\langle\sigma_{\rm ann}v\rangle$ (**left**) and lower limits on τ_χ (**right**), for secondary photons produced from different final state SM particles, from the Segue 1 observations with MAGIC.

5.1 Secondary photons from final state Standard Model particles

Figure 5 shows the upper limits on $\langle\sigma_{\rm ann}v\rangle$, together with the null hypothesis, 1σ and 2σ expectations, for annihilation into six different final states: quarks ($b\bar{b}$, $t\bar{t}$), leptons ($\mu^+\mu^-$, $\tau^+\tau^-$) and gauge bosons (W^+W^-, ZZ). All bounds are consistent with the no-detection scenario. For a more comprehensive overview, the $\langle\sigma_{\rm ann}v\rangle$ upper limits for the considered final states are shown in figure 6-left. A clear dependence between the shape of the expected

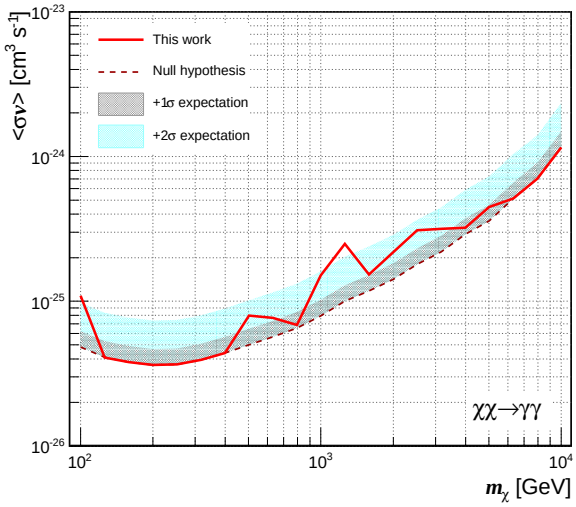

Figure 7: Upper limits on $\langle\sigma_{\rm ann}v\rangle$ for direct annihilation into two photons, as a function of m_χ, from the Segue 1 observations with MAGIC (solid line) and as expected for the case of no signal (dashed line), as well as for a signal of 1σ or 2σ significance (gray and light blue shaded areas, respectively).

photon spectrum and the derived constraints can be noticed: the strongest bound corresponds to the $\tau^+\tau^-$ channel ($\langle\sigma_{\rm ann}v\rangle \sim 1.2{\times}10^{-24}$ cm^3 s^{-1}), as it produces photons whose spectrum is the hardest at energies for which the sensitivity of MAGIC is at peak.

Similar considerations apply to the decaying DM scenarios: again, the most constraining lower limit on τ_χ from Segue 1 observations is obtained for the $\tau^+\tau^-$ channel, and is of the order of $\tau_\chi \sim 2.9{\times}10^{25}$ s.

5.2 Gamma-ray lines

Figure 7 shows the upper limits on $\langle\sigma_{\rm ann}v\rangle$ for direct annihilation of DM particles into two photons. For the considered m_χ range, the constraints are set between $3.6{\times}10^{-26}$ and $1.1{\times}10^{-24}$ cm^3 s^{-1}. In almost the entire considered mass range, the upper limits are within 1σ from the null hypothesis; the largest deviation is observed at $m_\chi \sim$1.3 TeV where the signal is slightly larger than 2σ. The probability that this is caused by random fluctuations of the background is relatively large ($\sim$5%) and hence not enough to be considered a hint of a signal[2]. On the other hand, should the excess be caused by gamma-rays from DM annihilation or decay, a detection at a 5σ significance level would require about 1000 hours of observations with a sensitivity comparable to the ones used here.

Upper limits on $\langle\sigma_{\rm ann}v\rangle$ from DM annihilation into photon and Z boson, for the considered DM masses, span the range between $7.8{\times}10^{-26}$ cm^3 s^{-1} and $2.3{\times}10^{-24}$ cm^3 s^{-1}. In the calculation of these limits we do not take into account the contribution of secondary photons originating from fragmentation and decay of Z, as the bound from the resulting continuous contribution is expected to be negligible compared to that from the line (figures 5 and 7). Furthermore, due to the finite width of the Z boson, the gamma-ray line is not monochromatic. The calculation of the consequent corrections to the $\langle\sigma_{\rm ann}v\rangle$ upper limits are beyond the scope of this paper; however, we note that, given the energy resolution of MAGIC, the

[2]The same reasoning applies to other excesses of similar magnitude calculated for other models studied in this section.

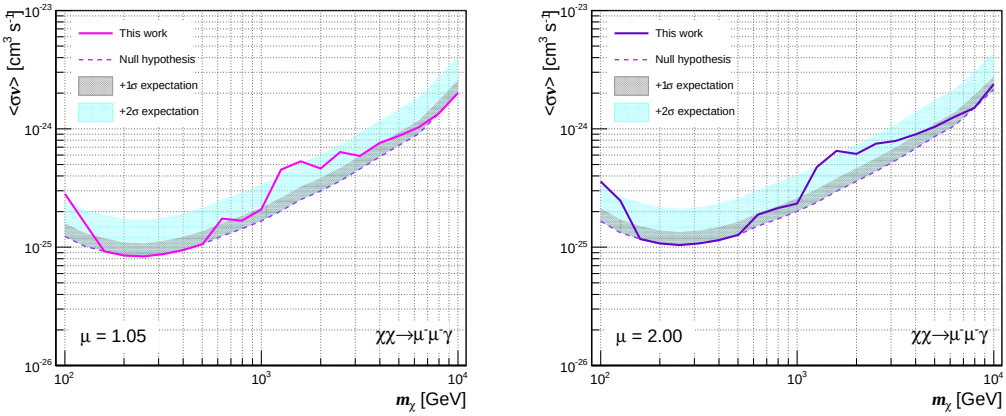

Figure 8: Upper limits on $\langle\sigma_{\rm ann}v\rangle$ for the $\mu^+\mu^-\gamma$ channel as a function of m_χ, from the Segue 1 observations with MAGIC (solid line), and as expected for the case of no signal (dashed line), or for a signal of 1σ or 2σ significance (gray and light blue shaded areas, respectively). The value of the mass splitting parameter μ is 1.05 (**left**) and 2.00 (**right**).

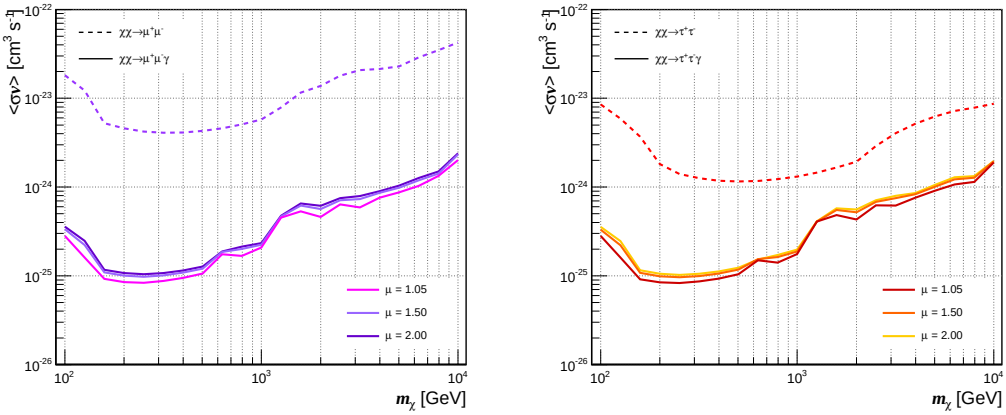

Figure 9: Upper limits on $\langle\sigma_{\rm ann}v\rangle$ for $\mu^+\mu^-\gamma$ (**left**) and $\tau^+\tau^-\gamma$ (**right**) final states, as a function of m_χ, for different values of the mass splitting parameter μ. Also shown are the exclusion curves for the annihilation without the VIB contribution (dashed line).

line broadening due to Z width ($\Gamma \sim 2.5$ GeV) is not expected to be of relevance in the considered m_χ range.

We also search for lines produced in DM decay. The derivation of such constraints is straightforward from the results of the annihilation scenario, so we limit our discussion on the matter to the comparison with bounds from other experiments, in section 6.2.1.

5.3 Virtual internal bremsstrahlung contribution

Here we consider the annihilation into leptonic channels with VIB contribution, and set limits on the total 3-body annihilation cross section. Figure 8 shows the $\langle\sigma_{\rm ann}v\rangle$ upper limits for the $\mu^+\mu^-\gamma$ channel, for different values of the mass splitting parameter, chosen such that the VIB contribution is significant with respect to the continuous one ($\mu = 1.05$ and 2.00, respectively). No positive detection can be claimed.

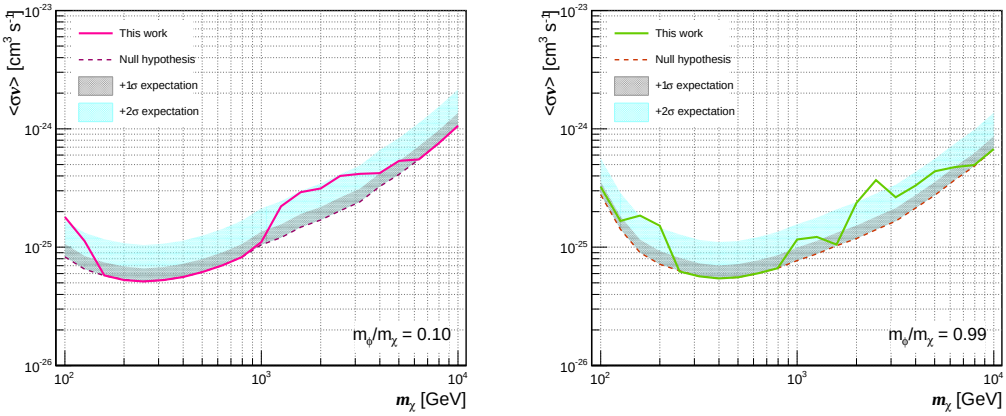

Figure 10: Upper limits on $\langle\sigma_{\rm ann}v\rangle$ for wide- ($m_\phi/m_\chi = 0.1$, **left**) and narrow ($m_\phi/m_\chi = 0.99$, **right**)-box scenarios, as a function of m_χ, from the Segue 1 observations with MAGIC (solid line), and as expected for the case of no signal (dashed line), as well as for the signal of 1σ or 2σ significance (gray and light blue shaded areas, respectively).

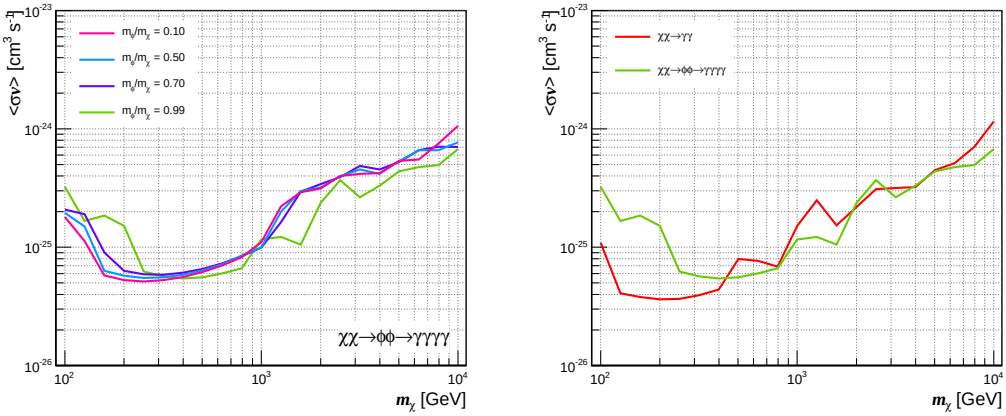

Figure 11: Comparison of upper limits on $\langle\sigma_{\rm ann}v\rangle$, as a function of m_χ, from the Segue 1 observations with MAGIC, for different ratios of scalar and DM particle masses (**left**), and of the narrow box scenario (m_ϕ/m_χ = 0.99) with a monochromatic gamma-ray line (**right**).

The comparison of these exclusion curves is better illustrated in figure 9-left: we see that, for several mass-splitting values (μ = 1.05, 1.50 and 2.00), the obtained limits are rather similar. This can be understood considering how the spectral shape of the VIB signal is practically independent of μ for such small mass-splitting parameter values. Still, it can be noticed that the most degenerate case, $\mu = 1.05$, provides the strongest limit, of $\langle\sigma_{\rm ann}v\rangle \sim 8.4\times10^{-26}$ cm^3 s^{-1} for $m_\chi \sim 250$ GeV. For illustration purposes, on the same plot we also show the $\langle\sigma_{\rm ann}v\rangle$ constraints calculated for the annihilation into the muon final state, but without the VIB contribution. In this particular case, the presence of VIB photons in the spectrum leads to almost two orders of magnitude more stringent bounds.

Analogous conclusions are reached for annihilation into the $\tau^+\tau^-\gamma$ final state (figure 9-right). The strongest limit in this case corresponds to $\langle\sigma_{\rm ann}v\rangle$ $\sim$8.3$\times10^{-26}$ cm^3 s^{-1}, for $m_\chi \sim 250$ GeV and $\mu = 1.05$. The relative contribution of the VIB 'bump' in this case is less significant than for the $\mu^+\mu^-\gamma$ channel, as the continuous gamma-ray spectrum of τ leptons

is of harder spectral slope.

5.4 Gamma-ray boxes

Here we consider the case of DM annihilation resulting in the production of four photons ($\chi\chi \to \phi\phi \to \gamma\gamma\gamma\gamma$). As for the DM decay scenarios, they are not covered here, given that the transformation of an upper limit on $\langle\sigma_{\rm ann}v\rangle$ to a lower limit on τ_χ is trivial, by making the replacement $\langle\sigma_{\rm ann}v\rangle/8\pi m_\chi^2 \to 1/m_\chi\tau_\chi$ in eq. (4.2) and $m_\chi \to m_\chi/2$ in eq. (4.3).

Figure 10 shows the $\langle\sigma_{\rm ann}v\rangle$ exclusion curves for extreme degeneracies when $m_\phi/m_\chi = 0.1$ and $m_\phi/m_\chi = 0.99$. In both cases, the strongest constraints are similar, of the order $\langle\sigma_{\rm ann}v\rangle \sim (5.1\text{–}5.4)\times10^{-26}$ cm^3 s^{-1}, for $m_\chi \sim 250$ GeV and ∼400 GeV, respectively.

Figure 11-left shows upper limits on $\langle\sigma_{\rm ann}v\rangle$ for the already mentioned extreme values of m_ϕ/m_χ (= 0.10, 0.99), as well as for some intermediate cases (m_ϕ/m_χ = 0.50, 0.70). As can be seen, with exception of the most narrow box scenario, all constraints are essentially the same, and only a factor few weaker than for the most degenerate configuration. This is understood given that the wide boxes compensate the dimmer amplitudes (with respect to the $m_\phi \approx m_\chi$ cases) by extending to higher energies, where the sensitivity of the telescopes is better.

For a more general view on the importance of box-shaped features, figure 11-right shows the upper limits on $\langle\sigma_{\rm ann}v\rangle$ from the most degenerate box model ($m_\phi/m_\chi = 0.99$) and from the line searches previously shown (figure 7). The obtained bounds are of the same order of magnitude, although the direct comparison between the two exclusion curves is not immediate: the line is centered at $E_\gamma = m_\chi$ and is normalized for 2 photons per annihilation, while the box-shaped feature is centered at $E_\gamma = m_\chi/2$ and is normalized for 4 photons. This is reflected as a shift of the exclusion curves in x and y coordinates.

For a more comprehensive overview, the most constraining bounds for all of the final state channels presented in this section are summarized in table 2.

6 Discussion

In this section, we discuss the advantages brought by the exploitation of the full likelihood analysis method, compare our results with other relevant experimental constraints and link them to the expectation from theoretical models.

6.1 Sensitivity gain from the full likelihood method

There are two aspects of the full likelihood analysis applied in this work that carry advantages for DM searches with IACTs: *i*) a sensitivity improvement due to the use of specific spectral signatures – such as those coming from DM annihilation and decay, and, *ii*) the combination of results from different data samples, e.g. obtained under different experimental conditions, becomes a trivial operation.

To quantify the improvement in sensitivity, we compute the *improvement factors* as defined in [28], i.e. the average ratio of the widths of the confidence intervals for the signal intensity, calculated by the full likelihood and conventional analysis methods, respectively, assuming a common CL. The confidence intervals are computed using fast Monte Carlo simulations of background events, with the same statistics and PDF as in the actual experimental conditions.

Table 3 shows the improvement factors obtained for signal from the $b\bar{b}$ and $\tau^+\tau^-$ annihilation channels and m_χ of 100 GeV, 1 TeV and 10 TeV. The calculations with the conventional

SECONDARY PHOTONS				
ANN	Final state	m_χ [TeV]	$\langle\sigma_{\rm ann}v\rangle$ [cm^3 s^{-1}]	Most constraining limit from dSphs
	$b\bar{b}$	1.78	5.44×10^{-24}	$m_\chi > 3.30$ TeV
	$t\bar{t}$	2.16	7.67×10^{-24}	no comparison possible
	$\mu^+\mu^-$	0.33	4.09×10^{-24}	$m_\chi > 0.29$ TeV
	$\tau^+\tau^-$	0.50	1.16×10^{-24}	$m_\chi > 0.55$ TeV
	W^+W^-	1.35	4.52×10^{-24}	$m_\chi > 2.77$ TeV
	ZZ	1.53	4.94×10^{-24}	no comparison possible
DEC	Final state	m_χ [TeV]	τ_χ [s]	Most constraining limit from dSphs
	$b\bar{b}$	20	2.54×10^{25}	full range
	$t\bar{t}$	20	1.97×10^{25}	no comparison possible
	$\mu^+\mu^-$	20	5.89×10^{24}	full range
	$\tau^+\tau^-$	20	2.89×10^{25}	full range
	W^+W^-	20	2.45×10^{25}	full range
	ZZ	20	2.58×10^{25}	no comparison possible
MONOCHROMATIC LINE				
ANN	Final state		m_χ [TeV]	$\langle\sigma_{\rm ann}v\rangle$ [cm^3 s^{-1}]
	$\gamma\gamma$		0.21	3.61×10^{-26}
	$Z\gamma$		0.25	7.82×10^{-26}
DEC	Final state		m_χ [TeV]	τ_χ [s]
	$\gamma\nu$		7.93	1.55×10^{26}
VIRTUAL INTERNAL BREMSSTRAHLUNG				
ANN	Final state	μ	m_χ [TeV]	$\langle\sigma_{\rm ann}v\rangle$ [cm^3 s^{-1}]
	$\mu^+\mu^-(\gamma)$	1.05	0.25	8.38×10^{-26}
		1.50	0.25	9.78×10^{-26}
		2.00	0.25	1.04×10^{-25}
	$\tau^+\tau^-(\gamma)$	1.05	0.25	8.28×10^{-26}
		1.50	0.25	9.62×10^{-26}
		2.00	0.25	1.02×10^{-25}
GAMMA-RAY BOXES				
ANN	Final state	m_ϕ/m_χ	m_χ [TeV]	$\langle\sigma_{\rm ann}v\rangle$ [cm^3 s^{-1}]
	$\gamma\gamma\gamma\gamma$	0.10	0.25	5.13×10^{-26}
		0.50	0.25	5.51×10^{-26}
		0.99	0.40	5.44×10^{-26}

Table 2: Summary of the strongest limits and corresponding m_χ, obtained from the Segue 1 observations with MAGIC, for various final states from DM annihilation (ANN) and decay (DEC). When applicable, it is stated for which range of considered m_χ these limits become the most constraining from dSph observations, among the published results.

method are done over both the optimized and the full energy range. The obtained improvement factor values are in agreement with the predictions made in [28], and imply a very significant boost in the sensitivity for DM searches: an improvement factor of f is equivalent to f^2 times more observation time.

Compared to our previous results of DM signals from Segue 1 [19], these results represent

m_χ	$b\bar{b}$		$\tau^+\tau^-$	
[GeV]	no opt.	opt.	no opt.	opt.
100	2.6	2.6	2.1	2.1
1000	1.9	1.9	3.1	1.7
10000	3.3	1.9	13.9	2.4

Table 3: Sensitivity improvement factors for the $b\bar{b}$ and $\tau^+\tau^-$ annihilation channels from the use of the full likelihood method over the conventional one, when the latter is calculated for the full (**no opt.**) or optimized (**opt.**) energy integration range.

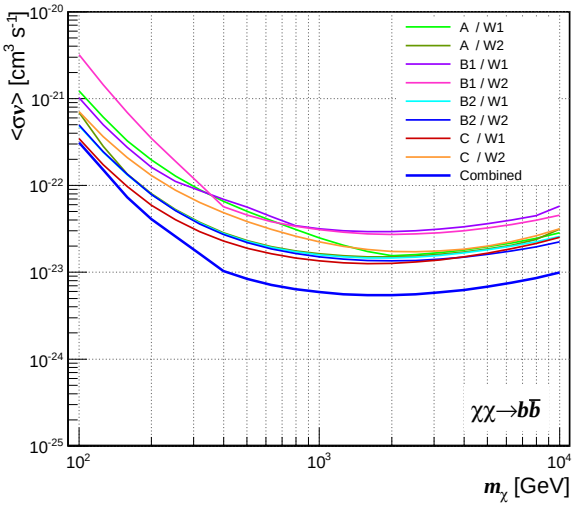

Figure 12: Upper limits on $\langle\sigma_{\rm ann}v\rangle$ for the $b\bar{b}$ annihilation channel, from individual wobble positions and different Segue 1 observational periods. Also shown is the limit from the combined likelihood analysis.

an overall improvement of about a factor of 10. This has been accomplished by the increase in the observation time of a factor ∼5.3 (i.e. a factor ∼2.3 better sensitivity), the operation of MAGIC as a stereoscopic system (a factor ∼2 better sensitivity with respect to single-telescope observations [46]), plus the improvement factor coming from the full likelihood analysis.

Furthermore, the full likelihood method allows a trivial merger of results obtained with different instruments or from different observational targets. As discussed in section 2, our data sample is divided into four periods with different instrumental conditions. In addition, for each period we use two different pointing positions, with slightly different background models. We have built dedicated individual likelihood functions for each of the eight different sub-periods, and merged them into a global likelihood following eq. (5.1) in [28], for our final results. The limits on $\langle\sigma_{\rm ann}v\rangle$ (assuming annihilation into the $b\bar{b}$ with Br = 100%) obtained by each of the eight considered sub-samples, compared to the global limit, are shown in figure 12.

6.2 Comparison with the results from other gamma-ray experiments

In the previous section we have estimated the $\langle\sigma_{\rm ann}v\rangle$ upper limits and τ_χ lower limits for various channels of DM annihilation/decay. Here, we put those constraints in context and compare them with the currently most stringent results from other gamma-ray observatories.

6.2.1 Secondary photons from final state Standard Model particles

Annihilation Figure 13 shows our $\langle\sigma_{\rm ann}v\rangle$ upper limits from DM annihilation into the $b\bar{b}$, $\mu^+\mu^-$, $\tau^+\tau^-$ and W^+W^- channels[3], compared with the corresponding constraints from *i*) joint analysis of 4 years of observations of 15 dSphs by *Fermi*-LAT [25]; *ii*) 112 hours of the GC Halo observations with H.E.S.S. (assuming generic $q\bar{q}$ final state, [47]); and *iii*) ∼48 hours of the Segue 1 observations with VERITAS [24]. Note, however, that the VERITAS results have been questioned in reference [28], where it is discussed why the VERITAS limits could be over-constraining by a factor two or more. Lastly, we also show the limits from ∼30 hours of the Segue 1 observations with MAGIC in single-telescope mode [19].

As seen from figure 13, for DM particles lighter than few hundreds GeV (depending on the specific channel), the strongest limits on $\langle\sigma_{\rm ann}v\rangle$ come from *Fermi*-LAT[4]; for higher m_χ values, the most constraining bounds are derived from the H.E.S.S. observations of the GC halo. We note, however, that the H.E.S.S. result heavily depends on the assumed DM profile, as it is sensitive to the difference in the DM-induced gamma-ray fluxes between the signal and background region, rather than to the absolute flux. In fact, by using a Navarro-Frenk-White (NFW) profile [48] instead of the Einasto one, the H.E.S.S. limit becomes a factor of ∼2 less constraining, or even weaker for very cored profiles with similar fluxes from the relatively close *ON* and *OFF* regions (figure 1 in [47]). This is particularly relevant considering possible uncertainties as, e.g., the effect of baryonic contraction in the GC that could have an important effect on the final DM profile [49].

Our $\langle\sigma_{\rm ann}v\rangle$ limits from 157.9 hours of the Segue 1 observations with MAGIC are the strongest limits from the dSphs observations with IACTs, and, for certain channels, also the most constraining bounds from dSph observations in general (table 2). For annihilation into the $b\bar{b}$ and W^+W^- final states, the MAGIC constraints complement those of the *Fermi*-LAT dSphs observations for $m_\chi > 3.3$ TeV and 2.8 TeV, respectively. For the leptonic channels, on the other hand, our limits become the most constraining above $m_\chi \sim 300$ GeV and ∼550 GeV, for annihilation into $\mu^+\mu^-$ and $\tau^+\tau^-$, respectively.

Decay Over the last couple of years, a lot of attention has been given to the decaying DM as a possible explanation of the flux excesses of high-energy positrons and electrons measured by PAMELA [52], *Fermi*-LAT [53], H.E.S.S [54] and AMS-02 [55]. The needed DM particle lifetime in such a case, $\tau_\chi > 10^{26}$ s, is much longer than the age of the Universe, so that the slow decay does not significantly reduce the overall DM abundance and, therefore, there is no contradiction with the astrophysical and cosmological observations.

Although DM decay has been disfavoured as the cause of the observed flux excesses (compared to astrophysical explanations; see, e.g., [56]), this scenario is an interesting subject by itself: e.g., if the DM particle is a gravitino, and small R-parity violation is allowed, the

[3]We do not show the limits for the $t\bar{t}$ and ZZ final states, as those channels are not discussed in the other mentioned studies.

[4]Note that *Fermi*-LAT results include each of the individual uncertainties on the astrophysical factors for the considered dSphs as nuisance parameters, whereas results by IACTs do not (since those limits scale trivially with J).

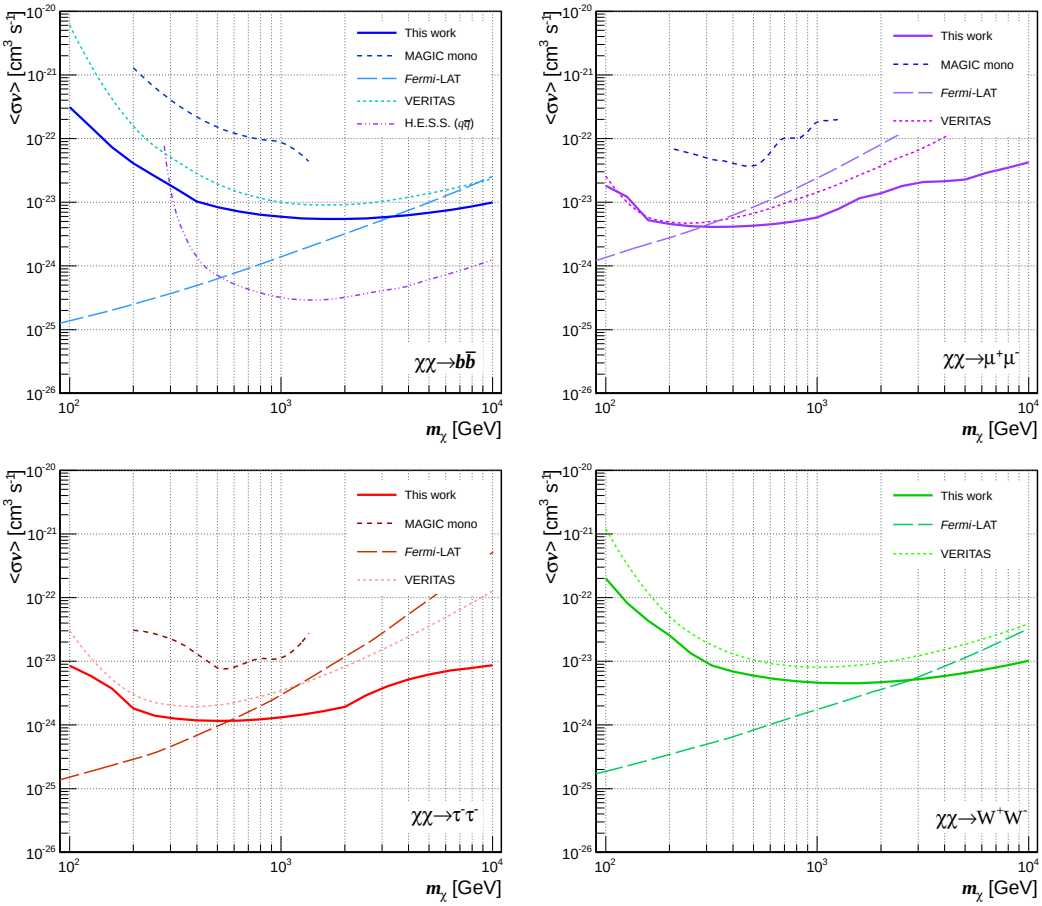

Figure 13: Upper limits on $\langle\sigma_{\rm ann}v\rangle$ for different final state channels (from top to bottom and left to right): $b\bar{b}$, $\mu^+\mu^-$, $\tau^+\tau^-$ and W^+W^-, from the Segue 1 observations with MAGIC (solid lines), compared with the exclusion curves from *Fermi*-LAT (long-dashed lines, [25]), H.E.S.S. (dot-dashed line, [47]), VERITAS (dotted lines, [24]) and MAGIC-I (dashed lines, [19]).

appropriate relic density through the thermal production is achieved, naturally leading to a cosmological history consistent with thermal leptogenesis and primordial nucleosynthesis [57].

The currently strongest constraints on τ_χ from gamma-ray observatories are derived from the *Fermi*-LAT diffuse gamma-ray data: the 2-year long measurements at energies between ∼1 and 400 GeV [58] exclude decaying DM with lifetimes shorter than 10^{25}–10^{26} s (depending on the channel) for m_χ between 10 GeV and 10 TeV. VERITAS also provides lower limits to τ_χ from ∼48 hours of Segue 1 observations [24] (albeit the already mentioned caveat regarding reliability of those results applies also in this case), excluding values below 10^{24}–10^{25} s (depending on the channel) for $m_\chi \simeq$ 1–10 TeV. Contrary to the annihilation case, the H.E.S.S. observations on the GC Halo are not competitive in the case of decay, as the expected gamma-ray fluxes are very similar in the signal and background regions. On the other hand, in [59] Cirelli et al. have shown that ∼15 hours of observations of the Fornax cluster with H.E.S.S. [60] could lead to the τ_χ lower limits of the order of $\sim(10^{24}$-$10^{26})$ s for m_χ between 1 and 20 TeV.

Figure 14 shows the results of this work, assuming the 2-body decay of scalar DM

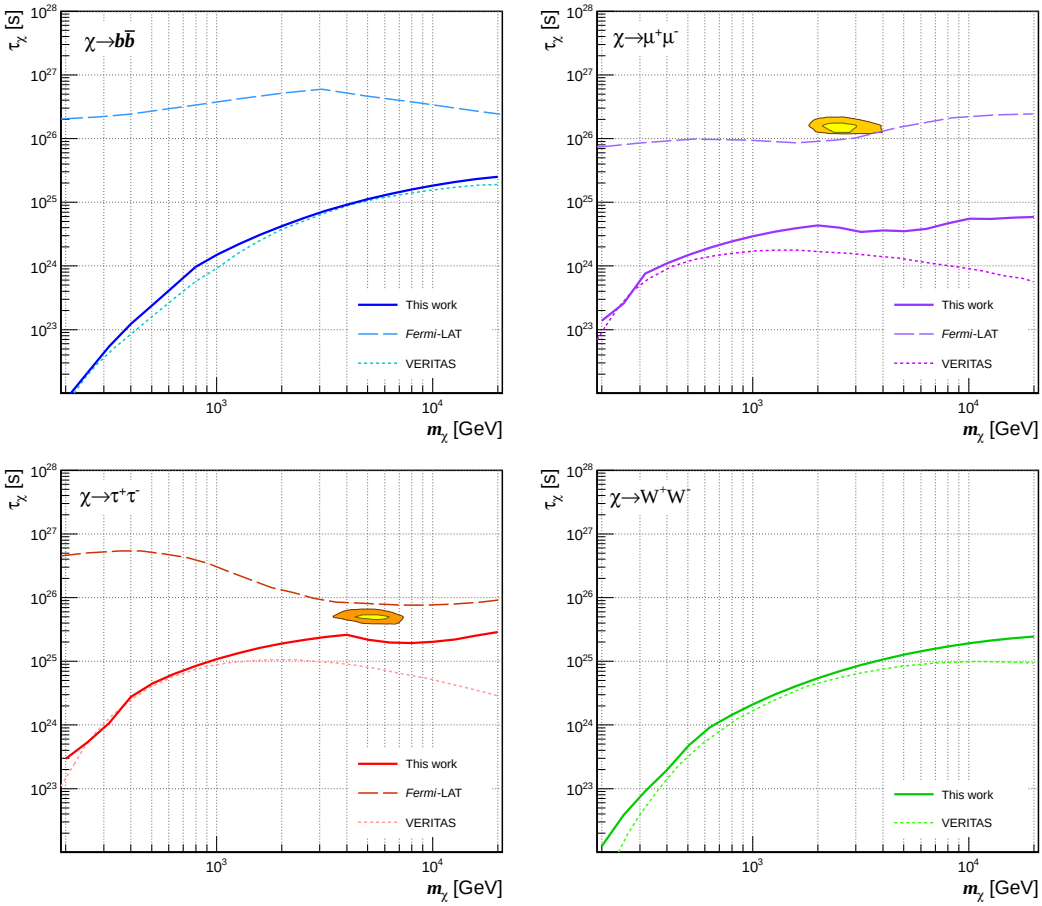

Figure 14: Lower limits on τ_χ for different final state channels (from top to bottom and left to right): $b\bar{b}$, $\mu^+\mu^-$, $\tau^+\tau^-$ and W^+W^-, from the Segue 1 observations with MAGIC (solid lines), compared with the exclusion curves from *Fermi*-LAT (long-dashed lines, [58]), and VERITAS (dotted lines, [24]). For the leptonic channels, $\mu^+\mu^-$ and $\tau^+\tau^-$, also shown are the regions that allow fit to the PAMELA, *Fermi*-LAT and H.E.S.S. cosmic-ray excess measurements, with 95% and 99.99% CL (orange and red regions, respectively; taken from [61]).

particle into quark-antiquark, lepton-antilepton and gauge boson pairs[5]. Our strongest limits correspond to $m_\chi = 20$ TeV, and are between $\sim 5.9\times10^{24}$ s and $\sim 2.9\times10^{25}$ s. Compared to the bounds from *Fermi*-LAT, for the lightest DM particles, the limits from this work are three-four orders of magnitude weaker; on the other hand, for more massive scenarios ($m_\chi >$ 1 TeV), the MAGIC bounds are a factor $\sim$30 to a factor $\sim$3 less constraining (for the muon and tau lepton final states, respectively). In all of the considered scenarios our results are more stringent than those of VERITAS (table 2). For the leptonic channels, we also show the regions that allow to fit the *Fermi*-LAT, PAMELA and H.E.S.S. cosmic-ray measurements [61], with 95% and 99.99% CL: our exclusion curves are factors $\sim$30 and $\sim$2 away from constraining those fits, for the $\mu^+\mu^-$ and $\tau^+\tau^-$ final states and masses $m_\chi = 2.5$ TeV and 5 TeV, respectively.

In general, observations of galaxy clusters are better suited than dSph for constraining

[5]For fermionic DM, decay channels such as $\chi \to l^\pm W^\mp$ and $Z\nu$ are possible, but these (in first approximation) can be analyzed as a combination of the corresponding 2-body scalar DM decay channels.

Figure 15: Upper limits on $\langle\sigma_{\rm ann}v\rangle$ for direct DM annihilation into two photons, from the Segue 1 observations with MAGIC (red line), compared with the exclusion curves from the GC region observations from *Fermi*-LAT (3.7 years, blue line [64]) and H.E.S.S. (112 hours, green line [65]). Also shown is the $\langle\sigma_{\rm ann}v\rangle$ value corresponding to the 130 GeV gamma-ray line (violet triangle, [66]).

τ_χ, due to the linear dependence of $J_{\rm dec}$ with the density ρ and the great amount of DM present in this kind of objects. This is reflected in the fact that the predicted limits for ∼15 hours observations of Fornax are of the same order of the ones we obtain for ∼160 hours of Segue 1 data [59].

6.2.2 Gamma-ray lines

The importance of the detection of gamma-ray lines from DM annihilation or decay can not be overestimated: not only would a line be a firm proof of DM existence, it would also reveal important information about its nature. This is why this feature has been so appealing, and many searches for a hint of it have been conducted so far, in galaxy clusters [62], Milky Way dSph satellites [63], and in the GC and Halo [64, 65]. In addition, it is worth mentioning that there is a recently claimed hint of a line-like signal at ∼130 GeV in the *Fermi*-LAT data of the GC region [43, 66]: if the observed signal originates from direct DM annihilation into two photons, the WIMP particle should have a mass of $m_\chi = 129\pm2.4^{+7}_{-13}$ GeV and an annihilation rate (assuming the Einasto profile) of $\langle\sigma_{\rm ann}v\rangle_{\gamma\gamma} = (1.27\pm 0.32^{+0.18}_{-0.28})\times10^{-27}$ cm^3 s^{-1}. Although this result could not be confirmed (nor disproved) by the *Fermi*-LAT Collaboration [64], the potential presence of such a feature has stirred the scientific community, and numerous explanations have appeared about its origin (for a review, see [67]).

Annihilation The currently strongest upper limits on spectral lines from DM annihilation are provided by the 3.7 years of observation of the Galactic Halo by *Fermi*-LAT [64], and 112 hours of the GC Halo region by H.E.S.S. [65]. The *Fermi*-LAT upper limits on $\langle\sigma_{\rm ann}v\rangle$ extend from ∼10^{-29} cm^3 s^{-1} at $m_\chi = 10$ GeV to ∼10^{-27} cm^3 s^{-1} at $m_\chi = 300$ GeV, while the H.E.S.S. bounds range between ∼10^{-27} cm^3 s^{-1} at $m_\chi = 500$ GeV and ∼10^{-26} cm^3 s^{-1} at $m_\chi = 20$ TeV.

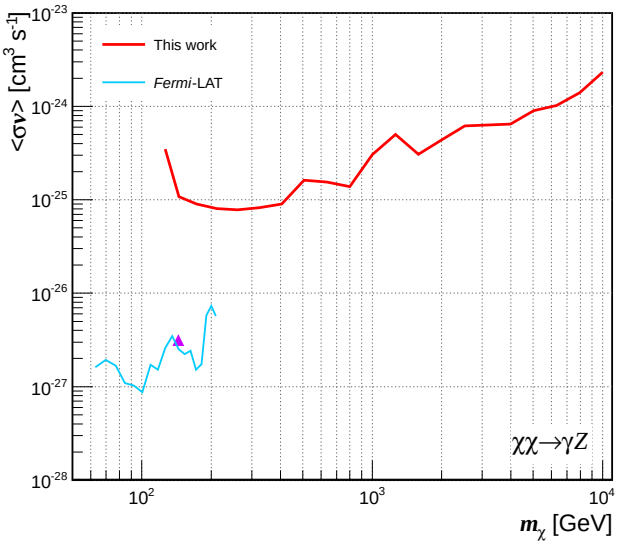

Figure 16: Upper limits on $\langle\sigma_{\rm ann}v\rangle$ for DM annihilation into a photon and a Z boson, from the Segue 1 observations with MAGIC (red line), compared with the exclusion curve from 2 years of the GC region observations with *Fermi*-LAT [68] (blue line). Also show is the $\langle\sigma_{\rm ann}v\rangle$ value corresponding to the 130 GeV gamma-ray line (violet triangle, [66]).

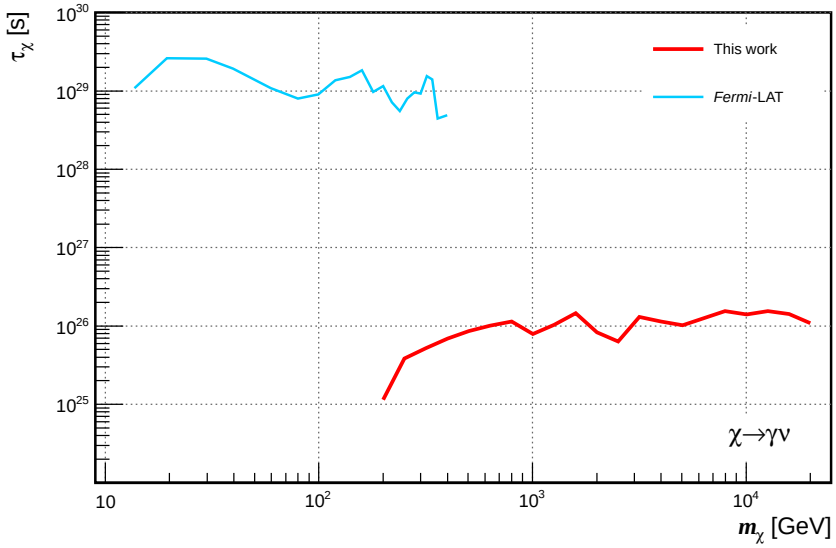

Figure 17: Lower limits on τ_χ for DM decay into a neutrino and a photon, from the Segue 1 observations with MAGIC (red line), compared with the exclusion curve from 2 years of the GC region observations with *Fermi*-LAT [68] (blue line).

Figure 15 shows our limits for the line search, assuming DM annihilation into two photons, compared to the described bounds from *Fermi*-LAT and H.E.S.S. The strongest constraint from MAGIC is obtained for $m_\chi = 200$ GeV, with $\langle\sigma_{\rm ann}v\rangle \sim 3.6{\times}10^{-26}$ cm^3 s^{-1}, which is about one order of magnitude higher than the *Fermi*-LAT limit, and a factor ∼30 above the sensitivity needed for testing the hint of a line at 130 GeV. For higher m_χ values, the H.E.S.S. limits are more constraining than ours by a factor ∼50 (as expected). We note, however, that similar considerations as those discussed in section 6.2.1 apply when comparing

the results of line searches from dSphs and Galactic Halo.

Results from line searches when DM particles annihilate into a photon and a Z boson are shown in figure 16: the strongest bound from this work corresponds to $\langle\sigma_{\rm ann}v\rangle \sim 7.8{\times}10^{-26}$ cm^3 s^{-1}, for $m_\chi \sim 250$ GeV. Compared to the constraints from 2 years of *Fermi*-LAT observations of the GC region [68], in the overlapping energy range, our limits are one-two order(s) of magnitude weaker. Also shown is the $\langle\sigma_{\rm ann}v\rangle$ estimate for the γZ explanation of the line-like feature at 130 GeV; the MAGIC upper limit is a factor ∼30 away from this value.

Decay We also use our search for spectral lines to constrain the properties of decaying DM. If the DM particle is a gravitino in R-parity breaking vacua, with $\tau_\chi \sim 10^{27}$ s or larger, it can decay into a photon and a neutralino, producing one monochromatic gamma-ray line at $E_\gamma \simeq m_\chi/2$. Searches for features of such origin have been conducted by the *Fermi*-LAT, in 2 years of observations of the GC region [68], setting lower limits on τ_χ of few$\times 10^{29}$ s up to $m_\chi \sim 600$ GeV, whereas, as explained in section 6.2.1, H.E.S.S. observations on the GC Halo are not sensitive for decaying DM searches.

Figure 17 shows our results compared to those from *Fermi*-LAT. Although the considered m_χ range extends well beyond the energies required for decay into W or Z bosons (that would consequently fragment into photons with continuous spectrum), here only the monochromatic emission is considered. MAGIC limits are almost three orders of magnitude less constraining than those of *Fermi*-LAT, but cover a complementary range of masses. This is expected, since (as discussed before), dSphs are suboptimal targets for DM decay signals. Our strongest bound is of the order of $\tau_\chi \sim 1.5{\times}10^{26}$ s for $m_\chi \sim 8$ TeV. The case of the decay of scalar DM into two photons is not considered here, as it is trivial to derive the τ_χ lower limits for that scenario: the gamma-ray signal would be the same as for the $\gamma\nu$ channel, only twice as strong.

6.3 Implications for models

Generating the correct WIMP relic density requires a DM annihilation cross section at the time of the freeze-out of $\langle\sigma_{\rm ann}v\rangle \simeq 3{\times}10^{-26}$ cm^3 s^{-1}. This value then constitutes a model-independent upper limit on $\langle\sigma_{\rm ann}v\rangle$ today, and sets the minimal sensitivity required to observe a DM annihilation signal. The constraints derived in this paper from deep observations of Segue 1 lie, in most cases, two orders of magnitude above the canonical value. Nevertheless, for some channels – notably in $\chi\chi \to \tau^+\tau^-$ – the very characteristic photon spectrum allows us to derive more constraining bounds. In particular, for $m_\chi \sim 500$ GeV the limit on $\langle\sigma_{\rm ann}v\rangle$ for tau final states lies just a factor of ∼40 away from the thermal cross section. However, it should be borne in mind that a signal is expected at $\langle\sigma_{\rm ann}v\rangle \simeq 3{\times}10^{-26}$ cm^3 s^{-1} when the annihilation cross section is s-wave dominated. Some well motivated DM scenarios suggest the p-wave dominated annihilation (see, e.g., [69]), and as such suppressed today by the velocity squared of the DM particles. If this is the case, the expected $\langle\sigma_{\rm ann}v\rangle$ can be five-six orders of magnitude smaller than the canonical value. Scenarios of this class include those where the DM particle is a Majorana fermion that annihilates into a light fermion, for example $\chi\chi \to \mu^+\mu^-$ or $\tau^+\tau^-$.

The expected rate of annihilations producing spectral features is also typically smaller than the canonical value. The direct production of two photons ($\chi\chi \to \gamma\gamma$) occurs at the one-loop level, hence the expected rate for a thermally produced WIMP is necessarily suppressed by a factor α^2, giving an annihilitation cross section which is, in most scenarios,

$\lesssim \mathcal{O}(10^{-30})$ cm^3 s^{-1}. Therefore, even if the limits on $\langle\sigma_{\rm ann}v\rangle$ for direct photon production are close to the thermal value, a sensitivity increase of at least two-three orders of magnitude is required in order to possibly observe a signal. For annihilations with VIB contribution, the rate is suppressed compared to the canonical value by the extra electromagnetic coupling and by the three-body phase space, amounting to a factor of $\sim \alpha/\pi$. Hence, observation of a gamma-ray signal from the final states $\mu^+\mu^-\gamma$ or $\tau^+\tau^-\gamma$ requires a sensitivity of $\langle\sigma_{\rm ann}v\rangle \sim \mathcal{O}(10^{-28})$ cm^3 s^{-1}, which is three orders of magnitude below the limits obtained in this paper. Lastly, the rate of annihilations producing gamma-ray boxes is a priori unsuppressed, since $\langle\sigma_{\rm ann}v\rangle$ for the process $\chi\chi \to \phi\phi$ can be as large as the thermal value, and the branching fraction $\phi \to \gamma\gamma$ can be sizable, even 1. For this class of spectral features, the limits are then only a factor of a few above the values for the cross section where a signal might be expected.

It should be kept in mind, however, that these results are somewhat conservative: no flux enhancements, due to possible boost factors, have been considered. In general, the uncertainties entering the expected fluxes are large enough so that potential surprises cannot be excluded.

7 Summary and conclusions

We have reported the results on indirect DM searches obtained with the MAGIC Telescopes using observations of the dSph galaxy Segue 1. The observations, carried out between January 2011 and February 2013, resulted in 157.9 hours of good-quality data, thus making this the deepest survey of any dSph by any IACT so far. In addition, this is one of the longest observational campaigns ever, with MAGIC or any other IACT, on a single, non-variable object. That imposes important technical challenges on data analysis, for which suitable and optimized solutions have been successfully designed and implemented.

The data have been analysed by means of the *full likelihood method*, a dedicated analysis approach optimized for the recognition of spectral features, like the ones expected from DM annihilation or decay. Furthermore, with this method, the combination of data samples obtained with different telescope configurations has been performed in a straightforward manner. This has resulted in sensitivity improvements by factors ranging between 1.7 and 2.6, depending on the DM particle mass and the considered annihilation/decay channel.

No significant gamma-ray excess has been found in the Segue 1 sample. Consequently, the observations have been used to set constraints on the DM annihilation cross section and lifetime, assuming various final state scenarios. In particular, we have computed limits for the spectral shapes expected for secondary gamma-rays from annihilation and decay into the SM pairs ($b\bar{b}$, $t\bar{t}$, $\mu^+\mu^-$, $\tau^+\tau^-$, W^+W^- and ZZ), for monochromatic gamma-ray lines, for photons produced by the VIB processes and for the spectral features from annihilation to gamma-rays via intermediate scalars. The calculations have been done in a model-independent way, by assuming a branching ratio of 100% to each of the considered final states. 95% CL limits to $\langle\sigma_{\rm ann}v\rangle$ and τ_χ have been obtained for m_χ in the 100 GeV $-$ 10 TeV range and 200 GeV $-$ 20 TeV, for annihilation and decay scenarios, respectively. The most constraining limits are obtained for DM annihilating or decaying purely into $\tau^+\tau^-$ pairs: $\langle\sigma_{\rm ann}v\rangle < 1.2 \times 10^{-24}$ cm^3 s^{-1} for $m_\chi \simeq 500$ GeV and $\tau_\chi > 3 \times 10^{25}$ s for $m_\chi \simeq 2$ TeV.

Studying different targets is of particular importance for indirect DM searches. On one hand, a certain confirmation of the DM signal, especially if it is a featureless one, can only come from observations of at least two sources. On the other hand, diversity among

observational targets is necessary, as searches in different objects are affected by different uncertainties. For instance, although most aspects of the general cold DM halo structure are resolvable from numerical approaches, the current knowledge and predictive power regarding its behaviour are limited by the complex interplay between the DM and baryonic components. It is still a long way until the effects baryons have on the DM distribution are fully perceived. This is particularly relevant for targets like the GC and Halo, or galaxy clusters, since their significant luminous content can influence the evolution of the DM component. Furthermore, there are also uncertainties coming from the presence of substructures in the halo, and the possible enhancements of the cross-section due to the quantum effects, that directly influence the value of the total expected flux. These uncertainties are large ($\mathcal{O}(10)$ or more) and their impact on halos may be different on different scales. Thus, diversification of the observational targets is the optimal strategy for the discovery.

Altogether, the results from this work represent an important step forward in the field of DM searches, significantly improving our previous limits from dSph galaxies and complementing the existing bounds from other targets.

Acknowledgments We would like to thank the Instituto de Astrofísica de Canarias for the excellent working conditions at the Observatorio del Roque de los Muchachos in La Palma. The support of the German BMBF and MPG, the Italian INFN, the Swiss National Fund SNF, and the Spanish MICINN is gratefully acknowledged. This work was also supported by the CPAN CSD2007-00042 and MultiDark CSD2009-00064 projects of the Spanish Consolider-Ingenio 2010 programme, by grant 127740 of the Academy of Finland, by the DFG Cluster of Excellence "Origin and Structure of the Universe", by the Croatian Science Foundation Project 09/176, by the DFG Collaborative Research Centers SFB823/C4 and SFB876/C3, and by the Polish MNiSzW grant 745/N-HESS-MAGIC/2010/0.

References

[1] P. A. R. Ade et al., *Planck 2013 results. XVI. Cosmological parameters* (2013) [arXiv:1303.5076]

[2] P. Hut, *Limits on masses and number of neutral weakly interacting particles*, *Phys. Lett.* **B69** (1977) 85-88

[3] G. Bertone (ed.). *Particle Dark Matter: Observations, Models and Searches. Cambridge University Press*, Cambridge, UK (2010) ISBN:978-0521763684

[4] H. P. Nilles, *Supersymmetry, Supergravity and Particle Physics*, *Phys. Rept.* **110** (1984) 1-162

[5] T. Appelquist, H. C. Cheng and B. A. Dobrescu, *Bounds on universal extra dimensions*, *Phys. Rev.* **D64** (2001) 035002 [arXiv:hep-ph/0012100]

[6] M. Cirelli, M. Fornengo and A. Strumia, *Minimal Dark Matter*, *Nucl. Phys.* **B753** (2006) 178-194 [arXiv:hep-ph/0512090]

[7] R. Bernabei et al., *First results from DAMA/LIBRA and the combined results with DAMA/NaI*, *Eur. Phys. J.*, **C56** (2008) 333-355 [arXiv:0804.2741]

[8] C. E. Aalseth et al., *Results from a Search for Light-Mass Dark Matter with a P-type Point Contact Germanium Detector*, *Phys. Rev. Lett.* **106** (2011) 31301 [arXiv:1002.4703]

[9] R. Agnese et al., *Dark Matter Search Results Using the Silicon Detectors of CDMS II*, (2013) [arXiv:1304.4279]

[10] R. Agnese et al., *CDMSlite: A Search for Low-Mass WIMPs using Voltage-Assisted Calorimetric Ionization Detection in the SuperCDMS Experiment*, (2013) [arXiv:1309.3259]

[11] E. Aprile et al., *Dark Matter Results from 225 Live Days of XENON100 Data*, Phys. Rev. Lett. **109** (2012) 181301 [arXiv:1207.5988]

[12] E. Aprile et al., *Limits on spin-dependent WIMP-nucleon cross sections from 225 live days of XENON100 data*, Phys. Rev. Lett. **111** (2013) 021301 [arXiv:1301.6620]

[13] D. S. Akerib et al., *First results from the LUX dark matter experiment at the Sanford Underground Research Facility*, (2013) [arXiv:1310.8214]

[14] S. Chatrchyan et al., *Observation of a new boson at a mass of 125 GeV with the CMS experiment at the LHC*, Phys. Lett. **B716** (2012) 30-61 [arXiv:1207.7235]

[15] D. Merritt et al., *Dark Matter Spikes and Annihilation Radiation from the Galactic Center*, Phys. Rev. Lett. **88** (2002) 191301 [arXiv:astro-ph/0201376]

[16] A. Pinzke, C. Pfrommer and L. Bergström, *Prospects of detecting γ-ray emission from galaxy clusters: cosmic rays and dark matter annihilations*, Phys. Rev. **D84** (2011) 123509 [arXiv:1105.3240]

[17] J. Albert et al., *Upper limit for gamma-ray emission above 140 GeV from the dwarf spheroidal galaxy Draco*, Astrophys. J. **679** (2008) 428-431 [arXiv:0711.2574]

[18] E. Aliu et al., *MAGIC upper limits on the VHE gamma-ray emission from the satellite galaxy Willman 1*, Astrophys. J. **697** (2009) 1299-1304 [arXiv:0810.3561]

[19] J. Aleksić et al., *Searches for dark matter annihilation signatures in the Segue 1 satellite galaxy with the MAGIC-I telescope*, JCAP **06** (2011) 035 [arXiv:1103.0477]

[20] F. Aharonian et al., *A search for a dark matter annihilation signal towards the Canis Major overdensity with H.E.S.S*, Astrophys. J. **691** (2009) 175-181 [arXiv:0809.3894]

[21] F. Aharonian et al., *Observations of the Sagittarius Dwarf galaxy by the H.E.S.S. experiment and search for a Dark Matter signal*, Astropart. Phys. **29** (2008) 55-62; Erratum-ibid.33: 274-275 (2010) [arXiv:0711.2369]

[22] A. Abramowski et al., *H.E.S.S. constraints on Dark Matter annihilations towards the Sculptor and Carina Dwarf Galaxies*, Astropart. Phys. **34** (2011) 608-616 [arXiv:1012.5602]

[23] V. A. Acciari et al., *VERITAS Search for VHE Gamma-ray Emission from Dwarf Spheroidal Galaxies*, Astrophys. J. **720** (2010) 1174-1180 [arXiv:1006.5955]

[24] E. Aliu et al., *VERITAS Deep Observations of the Dwarf Spheroidal Galaxy Segue 1*, Phys. Rev. **D85** (2012) 062001 [arXiv:1202.2144]

[25] M. Ackermann et al., *Dark Matter Constraints from Observations of 25 Milky Way Satellite Galaxies with the Fermi Large Area Telescope*, (2013) [arXiv:1310.0828]

[26] V. Belokurov et. al., *Cats and Dogs, Hair and A Hero: A Quintet of New Milky Way Companions*, Astrophys. J. **654** (2007) 897906, [arXiv:astro-ph/0608448]

[27] J. Simon et al., *A Complete Spectroscopic Survey of the Milky Way Satellite Segue 1: The Darkest Galaxy*, Astrophys. J. **733** (2011) 46-66 [arXiv:1007.4198]

[28] J. Aleksić, J. Rico and M. Martinez, *Optimized analysis method for indirect dark matter searches with imaging air Cherenkov Telescopes*, JCAP **10** (2012) 032 [arXiv:1209.5589]

[29] J. Sitarek et al., *Physics performance of the upgraded MAGIC telescopes obtained with Crab Nebula data*. In Proc. of the 33rd International Cosmic Ray Conference, Rio de Janeiro, Brazil (2013) [arXiv:1308.0141]

[30] J. Sitarek et al., *Analysis techniques and performance of the Domino Ring Sampler version 4 based readout for the MAGIC telescopes*, Nucl. Instrum. Meth. **A723** (2013) 109-120 [arXiv:1305.1007]

[31] D. Nakajima et al., *New Imaging Camera for the MAGIC-I Telescope*. In Proc. of the 33rd International Cosmic Ray Conference, Rio de Janeiro, Brazil (2013)

[32] V. P. Formin et al., *New methods for atmospheric Cherenkov imaging for gamma-ray astronomy 1: The False source method*, Astropart. Phys. **2** (1994) 137-150

[33] R. Zanin et al., *MARS, the MAGIC Analysis and Reconstruction Software*. In Proc. of the 33st International Cosmic Ray Conference, Rio de Janeiro, Brasil (2013)

[34] J. Albert et al., *Implementation of the Random Forest Method for the Imaging Atmospheric Cherenkov Telescope MAGIC*, Nucl. Instrum. Meth. **A588** (2008) 424-432 [arXiv:0709.3719]

[35] T. P. Li and Y. Q. Ma, *Analysis Methods for results in gamma-ray astronomy*, Astrophys. J. **272** (1983) 317-324

[36] W. A. Rolke and A. M. López and J. Conrad, *Limits and confidence intervals in the presence of nuisance parameters*, Nucl. Instrum. Meth. **A551** (2005) 493-503 [arXiv:physics/0403059]

[37] J. Aleksić. *Optimized Dark Matter Searches in Deep Observations of Segue 1 with MAGIC*. PhD thesis. Universitat Autónoma de Barcelona, Spain (2013)

[38] The ROOT Team, *TMinuit*, http://root.cern.ch/root/html/TMinuit.html, September 2013

[39] J. Cembranos et al., *Photon spectra from WIMP annihilation*, Phys. Rev. **D83** (2011) 083507 [arXiv:1009.4936]

[40] R. Essig et al., *Indirect Dark Matter Detection Limits from the Ultra-Faint Milky Way Satellite Segue 1*, Phys. Rev. **D82** (2010) 123503 [arXiv:1007.4199]

[41] L. E. Strigari et al., *Precise constraints on the dark matter content of Milky Way dwarf galaxies for gamma-ray experiments*, Phys. Rev. **D75** (2007) 083526 [arXiv:astro-ph/0611925]

[42] J. Hisano, S. Matsumoto and M. M. Nojiri, *Explosive Dark Matter Annihilation*, Phys. Rev. Lett. **92** (2004) 031303 [arXiv:hep-ph/0307216]

[43] T. Bringmann et al., *Fermi LAT Search for Internal Bremsstrahlung Signatures from Dark Matter Annihilation*, JCAP **07** (2012) 054 [arXiv:1203.1312]

[44] A. Ibarra, S. Lopez Gehler and M. Pato, *Dark matter constraints from box-shaped gamma-ray features*, JCAP **07** (2012) 043 [arXiv:1205.0007]

[45] J. F. Navarro et al., *The diversity and similarity of simulated cold dark matter haloes*, Mon. Not. Roy. Astron. Soc. **402** (2010) 21-34 [arXiv:0810.1522]

[46] J. Aleksić et al., *Performance of the MAGIC stereo system obtained with Crab Nebula data*, Astropart. Phys. **35** (2012) 435448 [arXiv:1108.1477]

[47] A. Abramowski et al., *Search for a Dark Matter Annihilation Signal from the Galactic Center Halo with H.E.S.S*, Phys. Rev. Lett. **106** (2011) 161301 [arXiv:1103.3266]

[48] J. F. Navarro, C. S. Frenk and S. D. White, *The Structure of Cold Dark Matter Halos*, Astrophys. J. **462** (1996) 563-575 [arXiv:astro-ph/9508025]

[49] F. Prada et al., *Dark Matter Annihilation in the Milky Way Galaxy: Effects of Baryonic Compression*, Phys. Rev. Lett. **93** (2004) 241301 [arXiv:astro-ph/0401512]

[50] A. Charbonnier et al., *Dark matter profiles and annihilation in dwarf spheroidal galaxies: prospectives for present and future gamma-ray observatories - I. The classical dSphs*, Mon. Not. Roy. Astron. Soc. **418** (2011) 1526[arXiv:1104.0412]

[51] T. Bringmann, M. Doro and M. Fornasa, *Dark Matter signals from Draco and Willman 1: prospects for MAGIC-II and CTA*, *JCAP* **01** (2009) 016[0809.2269]

[52] O. Adriani et al., *An anomalous positron abundance in cosmic rays with energies 1.5-100 GeV*, *Nature* **458** (2009) 607-609 [arXiv:0810.4995]

[53] A. A. Abdo et al., *Measurement of the Cosmic Ray e^+ plus e^- spectrum from 20 GeV to 1 TeV with the Fermi Large Area Telescope*, *Phys. Rev. Lett.* **102** (2009) 181101 [arXiv:0905.0025]

[54] F. Aharonian et al., *Probing the ATIC peak in the cosmic-ray electron spectrum with H.E.S.S*, *A&A* **508** (2009) 561 [arXiv:0905.0105]

[55] M. Aguilar et al., *First Result from the Alpha Magnetic Spectrometer on the International Space Station: Precision Measurement of the Positron Fraction in Primary Cosmic Rays of 0.5350 GeV*, *Phys. Rev. Lett.* **110** (2013) 141102

[56] B. Hooper, P. Blasi and P. Dario Serpico, *Pulsars as the sources of high energy cosmic ray positrons*, *JCAP* **01** (2009) 025 [arXiv:0810.1527]

[57] W. Buchmuller et al., *Gravitino Dark Matter in R-Parity Breaking Vacua*, *JHEP* **03** (2007) 037 [arXiv:hep-ph/0702184]

[58] M. Ackermann et al., *Constraints on the Galactic Halo Dark Matter from Fermi-LAT Diffuse Measurements Astrophys. J.* **761** (2012) 91-108 [arXiv:1205.6474]

[59] M. Cirelli et al., *Gamma ray constraints on Decaying Dark Matter*, *Phys. Rev.* **D86** (2012) 083506 [arXiv:1205.5283]

[60] A. Abramowski et al., *Search for Dark Matter Annihilation Signals from the Fornax Galaxy Cluster with H.E.S.S*, *Astrophys. J.* **750** (2012) 123 [1202.5494]

[61] M. Cirelli, P. Panci and P. D. Serpico, *Diffuse gamma ray constraints on annihilating or decaying Dark Matter after Fermi*, Nuc. Phys. **B840** (2011) 284-303 [arXiv:0912.0663]

[62] X. Huanga et al., *Constraints on the dark matter annihilation scenario of Fermi 130 GeV gamma-ray line emission by continuous gamma-rays, Milky Way halo, galaxy clusters and dwarf galaxies observations*, *JCAP* **11** (2012) 048 [1208.0267]

[63] A. Geringer-Sameth and S. M. Koushiappas, *Dark matter line search using a joint analysis of dwarf galaxies with the Fermi Gamma-ray Space Telescope*, *Phys. Rev.* **DD86** (2012) 021302 [arXiv:1206.0796]

[64] M. Ackermann et al., *Search for Gamma-ray Spectral Lines with the Fermi Large Area Telescope and Dark Matter Implications*, (2013) [arXiv:1305.5597]

[65] A. Abramowski et al., *Search for photon line-like signatures from Dark Matter annihilations with H.E.S.S*, *Phys. Rev. Lett.* **110** (2013) 041301 [arXiv:1301.1173]

[66] C. Weniger, *A tentative gamma-ray line from Dark Matter annihilation at the Fermi Large Area Telescope*, *JCAP* **08** (2012) 007 [arXiv:1204.2797]

[67] T. Bringmann and C. Weniger, *Gamma ray signals from dark matter: Concepts, status and prospects*, *Dark Universe* **1** (2012) 194-217 [arXiv:1208.5481]

[68] M. Ackerman et al., *Fermi LAT Search for Dark Matter in Gamma-ray Lines and the Inclusive Photon Spectrum*, *Phys. Rev.* **D86** (2012) 022002 [arXiv:1205.2739]

[69] H. Goldberg, *Constraint On The Photino Mass From Cosmology*, *Phys. Rev. Lett.* **50** (1983) 1419.

A Flux upper limits

As the Segue 1 observations with MAGIC have not resulted in a detection, differential and integral upper limits are calculated for the gamma-ray emission from the source, assuming a power law-shaped spectra of slope Γ, and by relying on the conventional analysis approach. The procedure and nomenclature used are those prescribed in [19].

The differential flux upper limits are estimated in energy bins ΔE as:

$$\frac{d\Phi^{\rm UL}}{dE}(E'_\star) = \frac{N_{\rm ex}^{\rm UL}(\Delta E)}{t_{\rm eff}} \frac{1}{\int_0^\infty A_{\rm eff}(E';\Delta E) S(E') dE'}, \tag{A.1}$$

where $S(E') = (E'/E'_\star)^\Gamma$ is the chosen power law spectrum. $E'_\star$ is the pivot energy for the particular energy bin, defined as:

$$E'_\star = \frac{\int_0^\infty E' S(E') A_{\rm eff}(E';\Delta E) dE'}{\int_0^\infty S(E') A_{\rm eff}(E';\Delta E) dE'}. \tag{A.2}$$

$A_{\rm eff}(E';\Delta E)$ is the effective area for events with measured energy within ΔE, as a function of true energy E'; $N_{\rm ex}^{\rm UL}$ is computed using global $N_{\rm ON}$, $N_{\rm OFF}$ and τ values and the conventional method [36], for a 95% CL and assuming a systematic uncertainty on the overall detection efficiency of 30%. $A_{\rm eff}(E';\Delta E)$ is computed for the entire sample as the weighted average of the effective areas of the four considered data sets, with weights being the corresponding observation times, i.e.:

$$A_{\rm eff}(E';\Delta E) = \frac{\sum_i \left(A_{{\rm eff}\,i}\ t_{{\rm eff}\,i}\right)}{t_{\rm eff}}, \tag{A.3}$$

where the index i runs over the different samples. Table 4 summarizes the upper limits in four (estimated) energy logarithmic bins, between 100 GeV and 10 TeV, for different assumed slopes of the power law-shaped signal emission ($\Gamma = -1.0$, -1.2, -1.5, -1.8, -2.0, -2.2 and -2.4). The results are also shown in figure 18.

The integral flux upper limits are calculated above a certain energy threshold $E_{\rm th}$ as:

$$\Phi^{\rm UL}(> E_{\rm th}) = \frac{N_{\rm ex}^{\rm UL}(E > E_{\rm th})}{t_{\rm eff}} \frac{\int_{E_{\rm th}}^\infty S(E') dE'}{\int_0^\infty A_{\rm eff}(E';\Delta E) S(E') dE'}, \tag{A.4}$$

The values of $N_{\rm ex}^{\rm UL}(E > E_{\rm th})$ and $A_{\rm eff}(E'; E > E_{\rm th})$ are obtained in a similar manner as described for the differential upper limits. Again, several power law spectra are assumed, with different slopes Γ. The results are summarized in table 5 and also shown in figure 19, where they are also compared with the values expected for the null hypothesis case, i.e. $N_{\rm ex}(E > E_{\rm th}) = 0$.

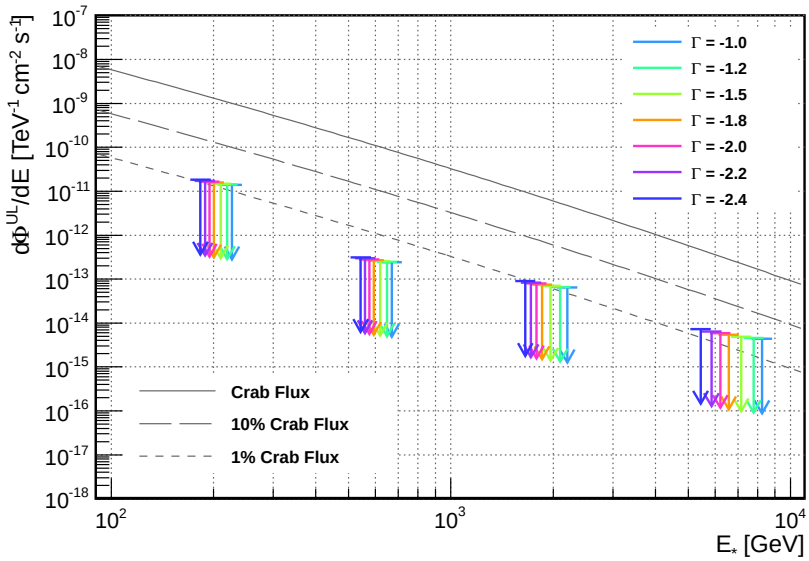

Figure 18: Differential flux upper limits from 157.9 hours of the Segue 1 observations with MAGIC, assuming a point-like source and a power law-shaped signal emission and different spectral slopes Γ. As a reference, the Crab Nebula differential flux (solid line, [46]) and its 10% and 1% fractions (long-dashed and dashed lines, respectively), are also drawn.

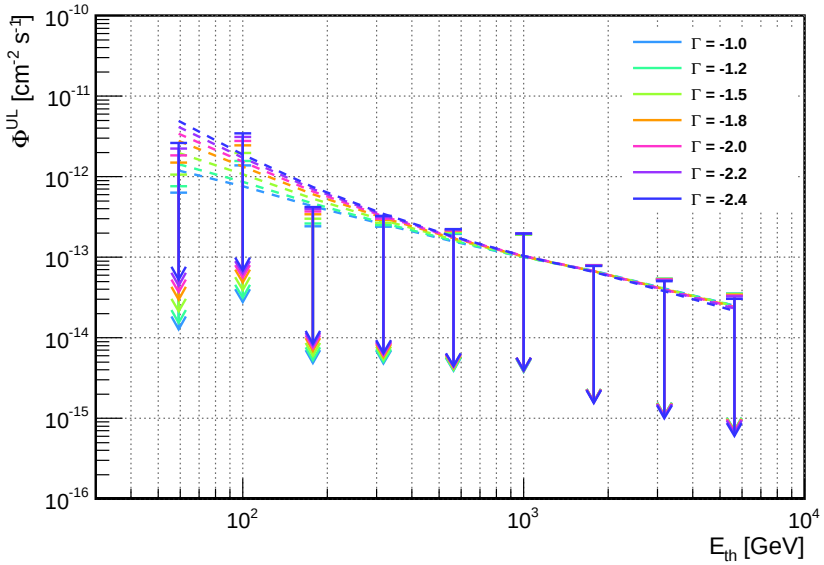

Figure 19: Integral flux upper limits from 157.9 hours of the Segue 1 observations with MAGIC, assuming a point-like source and a power law-shaped signal emission and different spectral slopes Γ. Dashed lines indicate the expectations for the null hypothesis case.

					$d\Phi^{\rm UL}/dE$ [TeV^{-1} cm^{-2} s^{-1}]						
ΔE [GeV]	$N_{\rm ON}$	$N_{\rm OFF}$	τ	$N_{\rm ex}^{\rm UL}$	$\Gamma=-1.0$	$\Gamma=-1.2$	$\Gamma=-1.5$	$\Gamma=-1.8$	$\Gamma=-2.0$	$\Gamma=-2.2$	$\Gamma=-2.4$
100−320	10996	10871	1.004	652.4	1.41×10^{-11}	1.44×10^{-11}	1.49×10^{-11}	1.57×10^{-11}	1.64×10^{-11}	1.72×10^{-11}	1.82×10^{-11}
320−1000	1606	1608	0.976	80.6	2.43×10^{-13}	2.48×10^{-13}	2.58×10^{-13}	2.71×10^{-13}	2.83×10^{-13}	2.96×10^{-13}	3.12×10^{-13}
1000−3200	341	314	1.001	109.2	6.40×10^{-14}	6.60×10^{-14}	6.99×10^{-14}	7.48×10^{-14}	7.89×10^{-14}	8.38×10^{-14}	8.97×10^{-14}
3200−10000	63	59	1.034	36.6	4.42×10^{-15}	4.57×10^{-15}	4.92×10^{-15}	5.42×10^{-15}	5.86×10^{-15}	6.44×10^{-15}	7.31×10^{-15}

Table 4: Differential flux upper limits from 157.9 hours of Segue 1 observations with MAGIC, in four energy bins and for several power law-shaped spectra.

					$\Phi^{\rm UL}$ [cm^{-2} s^{-1}]						
$E_{\rm th}$ [GeV]	$N_{\rm ON}$	$N_{\rm OFF}$	τ	$N_{\rm ex}^{\rm UL}$	$\Gamma=-1.0$	$\Gamma=-1.2$	$\Gamma=-1.5$	$\Gamma=-1.8$	$\Gamma=-2.0$	$\Gamma=-2.2$	$\Gamma=-2.4$
59.2	25804	26018	1.001	297.2	6.37×10^{-13}	7.66×10^{-13}	1.06×10^{-12}	1.49×10^{-12}	1.84×10^{-12}	2.23×10^{-12}	2.63×10^{-12}
100.0	13006	12832	1.001	708.0	1.39×10^{-12}	1.57×10^{-12}	1.96×10^{-12}	2.44×10^{-12}	2.78×10^{-12}	3.12×10^{-12}	3.44×10^{-12}
177.8	4869	4913	0.994	135.8	2.44×10^{-13}	2.63×10^{-13}	3.01×10^{-13}	3.43×10^{-13}	3.71×10^{-13}	3.98×10^{-13}	4.22×10^{-13}
317.2	2034	2007	0.983	144.9	2.41×10^{-13}	2.51×10^{-13}	2.70×10^{-13}	2.90×10^{-13}	3.03×10^{-13}	3.14×10^{-13}	3.25×10^{-13}
562.3	878	855	0.990	125.2	1.96×10^{-13}	1.99×10^{-13}	2.06×10^{-13}	2.13×10^{-13}	2.17×10^{-13}	2.21×10^{-13}	2.24×10^{-13}
1000.0	404	373	1.009	126.5	1.90×10^{-13}	1.91×10^{-13}	1.93×10^{-13}	1.96×10^{-13}	1.97×10^{-13}	1.97×10^{-13}	1.97×10^{-13}
1778.3	175	173	1.021	54.2	8.02×10^{-14}	8.02×10^{-14}	8.01×10^{-14}	7.99×10^{-14}	7.96×10^{-14}	7.90×10^{-14}	7.78×10^{-14}
3172.3	64	60	1.026	36.2	5.44×10^{-14}	5.42×10^{-14}	5.39×10^{-14}	5.34×10^{-14}	5.28×10^{-14}	5.19×10^{-14}	5.04×10^{-14}
5623.4	20	19	1.225	22.0	3.54×10^{-14}	3.52×10^{-14}	3.48×10^{-14}	3.42×10^{-14}	3.36×10^{-14}	3.25×10^{-14}	3.03×10^{-14}

Table 5: Integral flux upper limits from 157.9 hours of Segue 1 observations with MAGIC, for different energy thresholds and several power law-shaped spectra.